# 学位論文

## 結晶質相、非晶質・低結晶質相における
## ハロゲン, 11, 15, 16 族元素の存在状態と
## 原子レベル構造の解析、濃集過程・履歴の解読

**2019 年 3 月**

熊本大学大学院自然科学研究科

本宮　秀朋

**Abstract**

In the crystalline phase, the chemical composition of minerals is constant, or shows the solid solution relationship. Although it is a type of solid solution, minerals also contain trace elements in addition to elements that can be expressed in chemical formulae. By obtaining detailed structural information of various elements in minerals, it is possible to consider about the solid solution state and chemical bonding properties of the elements. Even in non- and low crystalline phases, it is possible to obtain information about the chemical state and coordination environment of the elements. In this doctoral thesis, as a preliminary study to consider the formation mechanism of epithermal gold and silver deposits, detailed information of elements in various mineral phases was obtained using optimal and up-to-date analytical methods. As elements related to the formation of epithermal deposits, Cu, Ag and Au of group 11 (IB), As and Sb of group 15 (VB), Te of group 16 (VIB), and F of group 17 (VIIB) (halogen) in the periodic table were studied limitedly. The research subjects are prosopite and petzite in crystalline phases, and Cretaceous-Tertiary boundary sediments with non- and low crystalline phases. These mineral phases include the aforementioned elements. In order to clarify the structure and state of unique atoms and ions and decipher the concentration process and history (especially in Cretaceous-Tertiary boundary sediments), the precise crystal structure and local structure of elements in various mineral phases were studied mainly using single-crystal X-ray diffraction and X-ray absorption fine structure (XAFS) spectroscopy. As an important factor to consider the origin of various mineral phases, the purpose of this study is to obtain new information on the detailed behavior of elements contained in various mineral phases, including the review of previous studies. Then, the basis for discussing the formation mechanism of gold and silver deposits and the concentration process of gold minerals is formed.

Prosopite is an alumino-fluoride of calcium mineral. For example, amphibole, mica and apophyllite include F and OH in the chemical composition. The substitution of $F^-$ and $(OH)^-$ occurs easily because each ionic radius is almost the same, and it is often represented as (F,OH) in the chemical formula of minerals. However, there are few studies that discussed in detail the state of the solid solution and the relation of order-disorder between F and OH in minerals. The chemical formula of prosopite is considered $CaAl_2(F,OH)_8$ or $CaAl_2F_4(OH)_4$. Pudovkina et al. (1973) performed single-crystal structure analysis of prosopite and refined the structure. However, they did not report the possible position of hydrogen atoms, and therefore, the details of hydrogen bonding and anionic site preference were not clarified. Prosopite is an interesting mineral in crystallography, it is necessary to clarify in detail the state of the

solid solution and/or the relation of order-disorder between F and OH in its structure. Therefore, the chemical compositions of prosopite were determined using scanning electron microscopy and energy-dispersive X-ray spectroscopy (SEM/EDS) and the crystal structure of prosopite including the position of hydrogen atoms was analyzed in detail using single-crystal X-ray diffraction.

From the chemical analysis, prosopite samples including a small amount of Cu and Sr as the substituents of Al and Ca were observed, respectively. The impurity substitution reaction, $Al^{3+} + (OH)^{-} \leftrightarrow Cu^{2+} + H_2O$, occurs at the cation sites. The positions of hydrogen atoms in the structure were determined at the position where residual electron density peaks appeared using the difference Fourier method. $F^{-}$ and $O^{2-}$ ions in prosopite are distributed at each F and O site in order. Based on the chemical analysis and structure refinement, we assumed the model in which $(OH)^{-}$ dissolution into F sites does not occur (but substitution of $F^{-}$ in (OH) sites slightly occurs). Therefore, we newly proposed that the chemical structural formula of prosopite is expressed as $CaAl_2F_4[(OH)_{4-x}F_x]$ ($x$ = 0.0–1.0).

Minerals in which gold is a major component have been confirmed to date, like calaverite $AuTe_2$, sylvanite $(Ag,Au)_2Te_4$, krennerite $(Au,Ag)Te_2$ and petzite $Ag_3AuTe_2$, besides native gold (Au). Gold and silver form extensive solid solutions in compounds. Gold minerals often include Sb, Bi, Se and Te and several gold and tellurium/antimony compounds are known. Gold-tellurium minerals such as calaverite and sylvanite have a simple chemical formula, but their crystal structures are far from simple and show incommensurate modulation under ambient conditions. Even the pure unsubstituted calaverite $AuTe_2$ shows a periodic ordered structure only under high-pressure conditions.

Petzite occurs with tellurides such as coloradoite and hessite in vein-type gold deposits. Thompson (1948, 1949) indicated that petzite is a compound with a definite silver-to-gold ratio, which suggests distinct ordered positions for the silver and gold atoms. This result corresponds to a three-dimensionally periodic non-modulated structure, unlike calaverite and sylvanite.

In this study, we performed a precise structural analysis of petzite single crystal samples and clarified the structure details such as the relation of order-disorder between Au and Ag atoms, the site occupancy on each site and the bonding character. In addition, XAFS analyses, in particular Au and Te $L_{III}$-edge X-ray absorption near edge structure (XANES) measurements were performed to investigate detailed bonding characteristics such as electrical properties. We also determined the Debye temperature and tried to predict the physical properties of petzite.

Our structure refinement essentially confirmed previous reports, but the absolute structure was actually the opposite with respect to the model. From Au XANES analysis, the chemical bonding of Au in petzite has a more pronounced metallic character than in other gold minerals. The Te XANES analysis indicates that the Te bonding in petzite shows a partially ionic character and the valence state is intermediate between metallic and anionic. We obtained Debye temperature $\theta_D$ values for Au, Ag and Te in petzite of 73.3, 101.1 and 108.5 K, respectively. These are significantly lower than the corresponding values in the pure metals (178, 221 and 152 K, respectively), reflecting the different binding forces in the telluride with respect to the respective metals.

The boundary between the Cretaceous and Tertiary geological ages at approximately 65.5 million years ago is called the K-T boundary (or recently the K/Pg boundary), and mass extinction occurred at that time. After unusually high concentrations of Ir in K-T boundary sediments were found by Alvarez et al. (1980), an asteroid impact was considered to have caused the K-T mass extinction. These Ir-rich K-T boundary sediments are found throughout the world (e.g., Stevns Klint in Denmark, Gubbio in Italy, Caravaca in Spain, and Woodside Creek in New Zealand). In addition to Pt-group elements such as Ir, the boundary sediments are also enriched with Cr, Co, Ni, Cu, Zn, As, and Sb. In the boundary sediments, Au and Se are also concentrated. Au-Sb (and Pt-As) minerals and gold halides have been confirmed as gold compounds. Therefore, there is a possibility that the bonding characteristics of elements in gold minerals such as petzite can be confirmed in K-T boundary sediments. Thus, Sb and As were selected as elements to be studied with respect to the concentration mechanism of gold minerals. Concerning the origins and concentration processes of elements such as Zn, As, and Sb, studies related to volcanism, and precipitation from seawater have been reported. In order to discuss in detail the origin and concentration process of As and Sb which have many unknown points, it is necessary to clarify the mineral phase containing these elements, and the structure and state of these elements. In the reddish brown sediment located in the lower part of the K-T boundary sediments from Stevns Klint in Denmark in this study area, it is considered that there are about half of non- and low crystalline phases that are difficult to identify by X-ray powder diffraction analysis. In the reddish brown sediment, the contents of Sb and As are in ppm units, and mineral phases containing them may be non- and low crystalline phases. Therefore, in order to obtain structural information of these elements, effective XAFS analysis for samples that are not crystalline is suitable. In this study, we determined the local structure around Sb and As atoms to obtain information about the chemical state and coordination environment of these atoms in K-T boundary sediments using XAFS analyses.

The Sb and As K-edge XANES patterns and threshold energies of K-T boundary sediments showed that the oxidation states of Sb and As are estimated to be $Sb^{5+}$ and $As^{5+}$, respectively. Sb and As in K-T boundary sediments are coordinated with oxide ions, and Sb and As exist in the same local structure positions as Sb and As in ferrihydrite (schwertmannite). The XANES spectra and radial structure function for Sb atoms also showed that Sb in K-T boundary sediments is stored in a $SbO_6$ octahedral coordination environment. Sb is considered to be coprecipitated with As and Fe ions, and Sb and As in K-T boundary sediments are incorporated in low crystalline ferrihydrite (schwertmannite) throughout precipitation and sedimentation. The environment at K-T boundary sediments resembles that of soil contaminated by Sb and As in local areas at the present time. However, in an unusual environment, such as widely distributed K-T boundary sediments in the world, unusually high concentrations of $Sb^{5+}$ and $As^{5+}$ could become an index of the soiling of the global environment with dust and ashes derived from asteroid impact ejecta falls.

The concentrations of Sb and As in K-T boundary sediments occur in the Earth's surface and oxidation environment, which are different from the formation process of hydrothermal deposits. When discussing mineralization of gold minerals, it is necessary to study complex ions in high-temperature solutions related to mineralization.

# 目次 Contents

題名: **結晶質相、非晶質・低結晶質相におけるハロゲン, 11, 15, 16 族元素の存在状態と原子レベル構造の解析、濃集過程・履歴の解読**

目次 Contents

# 第 1 章 Chapter 1

# General Introduction

General Introduction

鉱物の化学組成には一定であるもの、あるいは固溶関係を示すものがある（結晶質相）。また、鉱物中には、化学組成式で表すことのできる元素の他に微量に含まれる元素も存在する（固溶の一種）。鉱物における各種元素の詳細な構造情報の獲得により、元素の固溶状態、化学結合性等が考察可能である。非晶質・低結晶質相においても、元素の化学的状態や配位環境に関する情報を得ることができる。

過去に、熱水変質作用によるろう石鉱床に関して、主に元素分布に基づいた形成機構を研究していた。熱水性のろう石鉱床には金（、銀）鉱物が産出する例（例えば、菊池ら, 1982）がある。これは浅熱水性金鉱床と類似点があり、ろう石鉱床における元素の分布状態を調査中に、金鉱物の濃集・沈殿メカニズムに興味を持っていた。浅熱水性金鉱床において、金は溶液中でチオ錯体（やクロロ錯体）として存在し、温度、圧力、$H_2S$ 濃度、pH 条件の違いにより晶出するという報告がある（e.g., Seward, 1973; Reed and Spycher, 1984, 1985）。

この学位論文では、浅熱水性の金・銀鉱床の形成メカニズムを考察する予備的研究として、関連する元素の中で性質が似ている同族元素、あるいは結合の相性が良い元素どうしを考慮に入れて、11（IB）族元素の Cu, Ag, Au、15（VB）族元素の As, Sb、16（VIB）族元素の Te、17（VIIB）族（ハロゲン）元素の F (Fig. 1.1)にフォーカスして、最適かつ最新の分析・解析方法を用いて、多様な鉱物相の元素の詳細な情報を得ている。これらの元素を含む結晶質相の prosopite（水酸基を含むフッ化物）、petzite（金・銀・テルル鉱物）と非晶質・低結晶質相が存在する白亜紀-第三紀境界堆積物を研究対象として、主に単結晶 X 線回折法、XAFS（X 線吸収微細構造）法を用いて精密構造・局所構造解析を行った。そして、特殊な原子、イオンの構造・状態の解明や（特に白亜紀-第三紀境界堆積物において）濃集過程・履歴の解読を目指した。本研究では、多様な鉱物相の成因を考察する重要な要素として、先行研究の再検討も含めて、多様な鉱物相における含有元素の詳細な振る舞いに関して新しい知見を得ることを目的としている。そして、金・銀鉱床の形成と金鉱物の濃集メカニズムについて議論するための基盤を作る。

順を追って、以下にそれぞれの序論の詳細を示すことにする。

| 11(IB) | 12(IIB) | 13(IIIB) | 14(IVB) | 15(VB) | 16(VIB) | 17(VIIB) |
|---|---|---|---|---|---|---|
| | | 5**B** | 6**C** | 7**N** | 8**O** | 9**F** |
| | | 13**Al** | 14**Si** | 15**P** | 16**S** | 17**Cl** |
| 29**Cu** | 30**Zn** | 31**Ga** | 32**Ge** | 33**As** | 34**Se** | 35**Br** |
| 47**Ag** | 48**Cd** | 49**In** | 50**Sn** | 51**Sb** | 52**Te** | 53**I** |
| 79**Au** | 80**Hg** | 81**Ti** | 82**Pb** | 83**Bi** | 84**Po** | 85**At** |

**Figure 1.1.** 元素の周期表（一部）

結晶質相（単結晶構造解析）

prosopite の結晶構造精密化と化学式の決定（第 2 章）

Ca, Al の水酸基を含むフッ化物である prosopite は、花崗岩質、アルカリ貫入岩中、あるいは、火山性環境下、そして、F に富むグライゼン化作用や熱水作用における変質鉱物として、cryolite ($Na_3AlF_6$)等のようなアルミニウムフッ化物とともに産出する（e.g., Scheerer, 1857; Palache et al., 1951; Bailey, 1980; Young et al., 1997）。prosopite は、含まれる微量遷移金属イオンのため淡青緑色や淡赤色など様々な色を示す。後に述べる化学分析において、Al の一部が Cu と、Ca の一部が Sr と置換している試料が確認された。雲母、魚眼石等、化学組成に F と OH を含む鉱物、OH イオンが F によって置換される角閃石等が存在する (Table 1.1) が、F と OH はイオン半径がほぼ同じであることから置換しやすく、鉱物の化学式中では席選択を明らかにしていない(F,OH)として記されることも多い。しかし、詳細な F と OH 間の固溶状態や order-disorder の関係に関して議論した研究は少ない。prosopite の化学式は、$CaAl_2(F,OH)_8$ (e.g., Giacovazzo and Menchetti, 1969; Young et al., 1997)、あるいは、$CaAl_2F_4(OH)_4$ (e.g., Pudovkina et al., 1973)と表される。prosopite の結晶構造は、Giacovazzo and Menchetti (1969)によって初めて X 線回折法から得られた結果に基づいて決定された。Pudovkina et al. (1973) は、prosopite の単結晶構造解析を行い、構造を精密化している。しかし、彼らは、可能な水素原子位置を決定しておらず、よって、水素結合の詳細や陰イオンの席選択について明らかではなかった。このように、prosopite は、その構造中の

詳細な F と OH 間の固溶状態や order-disorder の関係に関して議論の余地があり、結晶化学的に興味深い鉱物である。よって、走査電子顕微鏡付属エネルギー分散型 X 線分光分析（SEM/EDS）法を用いて prosopite の化学組成を決定し、単結晶 X 線回折法を用いて詳細に水素原子位置を含む prosopite の結晶構造解析を行い、陽イオン席において一部置換する元素も含めて、これらに関して考察した。

**Table 1.1.** F と OH を含む鉱物の例

| |
|---|
| Amphibole group |
| Fluoro-edenite $\{Na\}\{Ca_2\}\{Mg_5\}(AlSi_7O_{22})(F,OH)_2$ |
| Potassic-fluoro-hastigsite $\{K\}\{Ca_2\}\{Fe^{2+}{}_4Fe^{3+}\}(Al_2Si_6O_{22})(F,OH)_2$ |
| Fluoro-pargasite $\{Na\}\{Ca_2\}\{Mg_4Al\}(Al_2Si_6O_{22})(F,OH)_2$ |
| Mica group |
| Biotite $K(Fe^{2+}/Mg)_2(Al/Fe^{3+}/Mg)([Si/Al]Si_2O_{10})(OH/F)_2$ |
| Fluorannite $KFe^{2+}{}_3(AlSi_3O_{10})(F,OH)_2$ |
| Fluorophlogopite $KMg_3(AlSi_3O_{10})(F,OH)_2$ |
| Apophyllite group |
| Fluorapophyllite-(K) $KCa_4(Si_8O_{20})(F,OH)\cdot 8H_2O$ |
| Hydroxyapophyllite-(K) $KCa_4(Si_8O_{20})(OH,F)\cdot 8H_2O$ |

結晶質相（単結晶構造解析、XAFS 法による局所構造解析）

petzite の結晶構造解析と XAFS 分析（第 3 章）

現在、30 種類近くの金を主成分とする鉱物が確認されている。自然金（Au）以外では例えば、calaverite $AuTe_2$, sylvanite $(Ag,Au)_2Te_4$, krennerite $(Au,Ag)Te_2$, petzite $Ag_3AuTe_2$ といった鉱物が産出する。これらは単独で産出するだけでなく、互いに共存し、他の金鉱物を伴って産出する。これら金鉱物に関する研究は比較的多くされている。金と銀は元素の周期表で coinage metals (貨幣金属) group に属し、化合物（鉱物）中で組成幅の広い固溶体を作る。そして、また、エレクトラムと呼ばれる合金も形成する。金鉱物は、しばしば Sb, Bi, Se, Te といった元素を含んでおり、いくつかの Au と Te あるいは Sb の化合物が知られている。

それらは、calaverite や sylvanite のように単純な化学式で表されるが、その結晶構造は常温常圧下では incommensurate (非整合)構造を示し、複雑である（Schutte and Boer, 1988; Pertlik, 1984; Reithmayer et al. 1993; Bindi et al., 2009; Bindi and Chpuis, 2017）。calaverite $AuTe_2$ は固溶体の端成分において、高圧条件下でのみ周期性、規則性構造となる（Reithmayer et al., 1993）。

petzite は、鉱脈型金鉱床でテルル化物に伴う。また、coloradoite HgTe や hessite $Ag_2Te$ と共生し、それらに intergrowth (連晶)として産出する（Frueh, 1959）。petzite は、Thompson (1948)によって初めて合成された。Frueh (1959)によってその構造が決定され、その後、Chamid et al. (1978)により精密化された。Thompson (1948, 1949)は、petzite は、区別された規則的な位置に Ag 原子と Au 原子が配置されていることを示唆する明確な Ag-Au 比を持つ化合物であることを示している。それは calaverite や sylvanite とは異なり、3 次元の周期性、non-modulated (非変調)構造に対応している。hessite には、低温型（β 相）と高温型（α 相）の 2 つの多形がある（Schneider & Schulz, 1993）。Frueh (1959)は、未公表であるが 483 ± 10 K で petzite の相転移を示す熱分析を引用している。Frueh (1959)によって提案されたモデルでは、Au 原子は 2 個の Te 原子（距離：2.61 Å）と 6 個の Ag 原子（距離：3.06 Å）に配位されている。Ag 原子は Te 原子に 4 配位され、Ag-Te 間距離は、二つが 2.92 Å で、もう二つは 2.96 Å である。Te 原子は 1 個の Au 原子（距離 : 2.61 Å）、3 個の Ag 原子（距離 : 2.92 Å）、そしてもう 3 個の Ag 原子（距離 : 2.96 Å）に配位されている。Au-Te 間距離が Ag-Te 間距離より短いのは、petzite 中で Au において 2 個が近くに隣接しているためであると説明している。

本研究では、petzite の単結晶試料の精密構造解析を行い、構造の詳細と各元素の各々のサイトにおける席選択性、結合状態の特徴を明らかにする。さらに、XAFS 法を用いた解析、特に吸収原子の価数、配位原子種や構造のゆがみ等の情報が得られる XANES（X 線吸収端近傍構造）スペクトル解析によって各元素の化学結合性を考察する。また、Debye 温度を決定し、物性の予測を試みた。

非晶質・低結晶質相（XAFS 法による局所構造解析）

隕石衝突時の特殊環境下で生成した堆積物（白亜紀-第三紀境界堆積物）( : 堆積物中の濃集元素、特に Sb, As の XAFS 解析と濃集過程の推定）（第 4 章）

約 6550 万年前の中生代白亜紀と新生代古第三紀の地質年代境界は、K-T 境界あるいは最近では K/Pg 境界と呼ばれ、そこでは恐竜等の生物の大量絶滅のイベントがあったことが知られている。Alvarez et al. (1980) は、Stevns Klint in Denmark と Gubbio in Italy の K-T 境界堆積物において地殻中にほとんど存在しない Ir が異常濃集している事実より、生物の大量絶滅の原因は隕石衝突時、そして、その後一定期間の地球規模の環境変化によるものであると革新的な提案を

した。その後、この Ir が異常濃集している K-T 境界堆積物層は、深海底を含め世界各地（例えば、Stevns Klint in Denmark, Gubbio in Italy の他、Caravaca in Spain, Woodside Creek in New Zealand 等）で発見されている。また、K-T 境界堆積物中には、隕石衝突の証拠となる衝撃変成石英、テクタイト、スフェリュール等も確認されている。この境界堆積物中には Ir のような白金族元素の他に Cr, Co, Ni, Cu, Zn, As, Sb といった元素も濃集していることが報告されている（Strong et al., 1987; Schmitz, 1992）。この特徴的な元素の濃集傾向について、Cr, Ni は主に隕石物質由来、Cu, Zn, As, Sb は地球物質起源の impact ejecta（衝突時の噴出物）由来だと考えられている（Strong et al., 1987; Schmitz, 1992）。他に Au, Se 等も濃集しており、金の化合物について天然では Au-Sb 系（、Pt-As 系）鉱物、また、Au のハロゲン化物が存在するので、鉱床ではないが K-T 境界堆積物中で petzite 等の金鉱物の元素の結合の特徴が確認できる可能性がある。これを踏まえて金の濃集メカニズムにも関連して、Sb, As に焦点を当てた。非隕石起源によるところが大きいとされる Zn, As, Sb の起源、濃集過程に関して、火山活動に関係する研究（Officer and Drake, 1985）や海水中からの沈殿によるとされること（Gilmour and Anders, 1989; Schmitz, 1992）が報告されている。しかし、不明な点が多い As, Sb の起源、濃集過程の詳細な議論のためには、それらの元素が含まれる鉱物相やその形態を明らかにする必要がある。例えば、Denmark の Stevns Klint の K-T 境界堆積層下部で Ir の含有量がピークである赤色堆積物中の主要構成鉱物は、X 線粉末回折分析では、smectite (montmorillonite), calcite, 少量の quartz, goethite である (Fig. 1.2)。この赤色堆積物中には、XRD 分析で同定困難な非晶質相や低結晶質成分が半分程度存在していると考えられる。（平均地殻濃度に比べ約 10 から 100 倍程度濃集しているが）Sb, As の含有量は ppm オーダーと微量であり、また、それらを含む鉱物相は非晶質・低結晶質の可能性がある。よって、これらの元素の構造的情報を得るためには、長距離秩序を必要とせず、結晶質でなくてもよい（試料の相に関係しない）試料に対して有効な XAFS 法を用いた解析が適している。我々の研究室では、これまでに XAFS 法を用いて Denmark の Stevns Klint の K-T 境界堆積物中の As, Zn, Ca, Cr, Mn, Fe, Ni, Zr, Ti の局所構造解析を行い、次に示すように、各元素の構造情報を得て、堆積環境の推定を行っている。局所構造に関して、Zn は willemite に似たフレームワーク構造中で $ZnO_4$ 四面体席を占め、海水のような高い pH 条件で沈殿したこと; Zr, Ti は隕石衝突におけるガラス構造を保持しており、急速な温度変化等の履歴を残すこと; Ca, Cr, Mn, Fe, Ni は堆積時の風化、続成作用、生物活動の影響を受けていることをそれぞれ提案、明らかにしている（Sakai et al., 2007; Okube et al., 2012; Tobase et al., 2015, 2019; Miyano et al., 2016）。同様に、XAFS 法を用いて Sb, As の局所構造解析を行い、それらの化学的状態や配位環境に関する情報を得て、K-T 境界堆積物

層中における Sb, As の形態および濃集鉱物相、また、濃集過程を議論することは、微量元素の詳細な分析・解析というミクロな視点からではあるが、隕石衝突時とその後の地球環境の推定に重要な研究手法の一つであると考える。

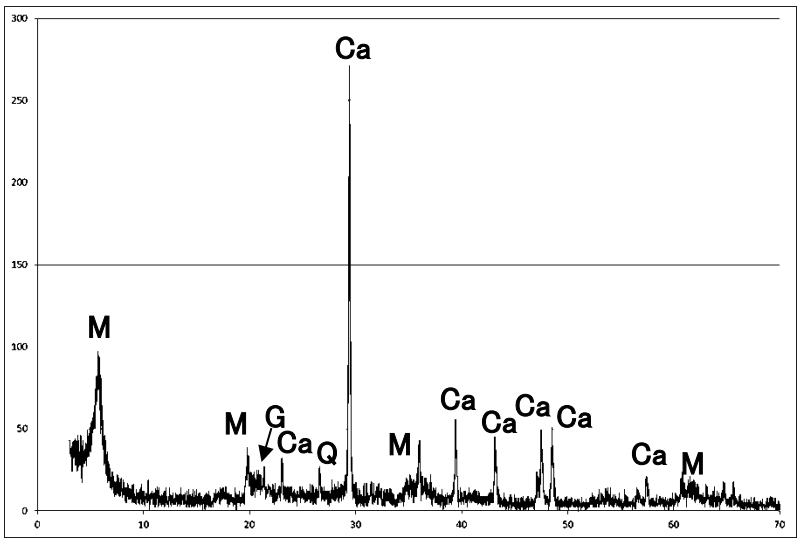


**Figure 1.2.** 赤色堆積物試料の X 線粉末回折図

なお、この学位論文は、日本文での記載を基本としているが、第 1 章（General Introduction）と第 5 章（General Conclusion）以外の、以下の第 2、3、4 章は、各章を形作る上で、同時に進めていた、先に投稿、受理された学術論文（英文）が重要なウエイトを占めているため、すべて英文で書いている。

第 2 章 Chapter 2 Crystal structure refinement and chemical formula of prosopite（prosopite の結晶構造精密化と化学式の決定）
第 3 章 Chapter 3 Crystal structure and XANES investigation of petzite, $Ag_3AuTe_2$（petzite の結晶構造解析と XAFS 分析）
第 4 章 Chapter 4 XAFS study of Sb and As in Cretaceous-Tertiary boundary sediments [隕石衝突時の特殊環境下で生成した堆積物（白亜紀-第三紀境界堆積物）（：堆積物中の濃集元素、特に Sb, As の XAFS 解析と濃集過程の推定）]

# 第 2 章 Chapter 2

# Crystal structure refinement and chemical formula of prosopite

# prosopite の結晶構造精密化と化学式の決定

## 2.1. INTRODUCTION

Prosopite, $CaAl_2(F,OH)_8$, an alumino-fluoride of calcium mineral, commonly occurs in association with aluminum fluoride minerals such as cryolite, $Na_3AlF_6$, and thomsenolite, $NaCaAlF_6•(H_2O)$, in granitic, alkaline intrusive, or volcanic environments, and is an alteration product after F-rich greisenization and hydrothermal processes (e.g., Scheerer, 1857; Palache et al., 1951; Bailey, 1980; Young et al., 1997). Prosopite usually appears in a variety of colors such as turquoise or pale red owing to the presence of a small amount of transition metal ions. The chemical formula of prosopite is considered $CaAl_2(F,OH)_8$ (e.g., Giacovazzo and Menchetti, 1969; Young et al., 1997) or $CaAl_2F_4(OH)_4$ (e.g., Pudovkina et al., 1973). The crystal structure of prosopite was determined based on the results of X-ray diffraction interpretation for the first time by Giacovazzo and Menchetti (1969). Pudovkina et al. (1973) performed single-crystal structure analysis of prosopite and refined the structure with distinction of F and (OH) sites as $CaAl_2F_4(OH)_4$. However, they did not report the possible position of hydrogen atoms, and therefore, the details of hydrogen bonding and anionic site preference were not elucidated. In this study, we determined the chemical compositions of prosopite using scanning electron microscopy and energy-dispersive X-ray spectroscopy (SEM/EDS) and analyzed the crystal structure of prosopite including the position of hydrogen atoms in detail using single-crystal X-ray diffraction. We investigated the relation between the substituted quantity of $F^-$ for $(OH)^-$ in prosopite and the structure of prosopite in order to clarify the state of the solid solution and/or the relation of order–disorder between $F^-$ and $(OH)^-$ in prosopite.

## 2.2. EXPERIMENTS

### 2.2.1. Chemical analysis

The prosopite samples used for the measurement were obtained from Zacatecas in Mexico (sample No. 1), Ivigtut in Greenland (Kingdom of Denmark, sample Nos. 2 and 3) and Katugin deposit in Eastern Siberia (Russia, sample No. 4). The chemical compositions were determined with multiple grains of each sample using JEOL SEM (JSM-7001F operated by 15 kV, 0.5 nA) equipped with Oxford EDS (INCA SYSTEM). The number of grains analyzed and analytical points were 3 and 19 (sample No. 1), 5 and 54 (sample No. 2), 5 and 31 (sample No. 3) and, 2 and 29 (sample No. 4), respectively. The following standard materials were employed: $CaF_2$ for F, $Al_2O_3$ for Al, $CaSiO_3$ for Ca, copper metal for Cu, and $SrTiO_3$ for Sr. The chemical formula was determined considering that the total number of charges (w.r.t. $Ca^{2+}$, $Sr^{2+}$, $Al^{3+}$, and $Cu^{2+}$) is eight, and the unanalyzed anions are assumed to be $(OH)^-$.

The specimens included a small amount of Cu and Sr as the substituents of Al and Ca, respectively (Table 2.1). The impurity substitution reaction, $Al^{3+} + (OH)^- \leftrightarrow Cu^{2+} + H_2O$, occurs at the cation sites. The empirical formulae as the means of chemical compositions are $Ca(Al_{1.98}Cu_{0.03})F_4[(OH)_{3.84}F_{0.16}]$ (Zacatecas sample No. 1), $(Ca_{0.96}Sr_{0.04})Al_{2.00}F_4[(OH)_{3.72}F_{0.28}]$ (Ivigtut sample No. 2), $(Ca_{0.93}Sr_{0.04})Al_{2.02}F_4[(OH)_{3.56}F_{0.44}]$ (Ivigtut sample No. 3), and $Ca_{0.98}Al_{2.01}F_4[(OH)_{3.70}F_{0.30}]$ (Katugin sample No. 4). Figure 2.1 shows the histograms of the measured amount (frequency) of fluorine content as apfu (atoms per formula unit). Textural and compositional variations such as chemical zoning were not observed in the

analysis of the multiple analytical points in a grain of each sample. As shown in Figure 2.1, the frequency distribution of fluorine content is not a normal distribution. Thus, the chemical compositions are obtained from the arithmetic average values and the errors are not considered (Table 2.1). The ratio of Ca and Al, which are cations in the empirical formula, as the means of chemical compositions of four samples is almost the same as that of the ideal chemical formula of prosopite. The fluorine content was between 4 and 5 and the quantity of maximum substitution of $F^-$ for $(OH)^-$ in prosopite was estimated to be 25% (Table 2.1 and Fig. 2.1).

**Table 2.1.** Mean of chemical compositions as apfu of all prosopite samples (No. 1 to No. 4)

| | Sample No. 1 | Sample No. 2 | Sample No. 3 | Sample No. 4 |
|---|---|---|---|---|
| F | 4.16 | 4.28 | 4.44 | 4.30 |
| Al | 1.98 | 2.00 | 2.02 | 2.01 |
| Ca | 1.00 | 0.96 | 0.93 | 0.98 |
| Cu | 0.029 | — | — | — |
| Sr | — | 0.04 | 0.04 | — |
| $OH^*$ | 3.84 | 3.72 | 3.56 | 3.70 |

* Unanalyzed anion content obtained by subtracting F content from that of eight anions is assumed to be that of $(OH)^-$.

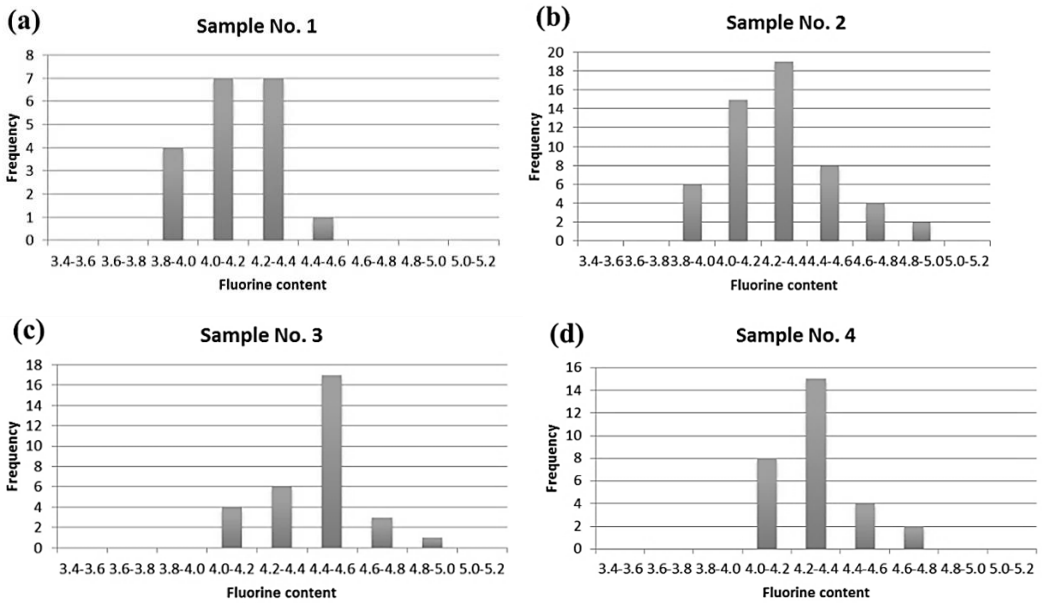


**Figure 2.1.** Histograms of measured amount (frequency) of fluorine content as apfu of the four prosopite samples. (a) Zacatecas, Mexico. (b) Ivigtut, Greenland. (c) Ivigtut, Greenland. (d) Katugin deposit, Eastern Siberia, Russia.

### 2.2.2. Crystal structure refinement

The crystal structure of prosopite (sample No. 2) was analyzed using single-crystal X-ray diffraction. The crystalline qualities of the single-crystal specimens were evaluated using a four-circle diffractometer at the BL-10A beam line of the Photon Factory, High Energy Accelerator Research Organization, KEK, Japan, using high-resolution monochromatized synchrotron X-ray radiation. The structure refinement was performed using reflection intensity data obtained using a Rigaku X-ray diffractometer (Vari-MAX-RAPID) with an imaging plate (graphite-monochromatized

Mo*K*α radiation, λ = 0.71069 Å) and a rotating anode X-ray tube, at Tohoku University. Focused Mo*K*α radiation was utilized and the conventional oscillation technique was applied. After Lorentz and polarization corrections, an absorption correction was performed by using the integration method based on the shape of the specimen (Higashi, 1995). The space group *C*2/*c* was adopted based on the systematic absence conditions of the observed diffraction intensity data. Accordingly, 2944 reflection intensities were measured. The experimental details and crystallographic data are summarized in Table 2.2.

The crystal structure refinement was carried out using SHELXL97 program (Sheldrick, 1997). The crystal structure of prosopite was refined to the *R* value of 0.0185 (*wR*2 = 0.0554) using 791 unique reflections with $|F_o| > 4\sigma(|F_o|)$. Scattering factors for neutral atoms and anomalous dispersion coefficients were obtained from International Tables for Crystallography, Volume C (1992). In the structural refinement, the Ca site was considered to be fully occupied by Ca and Sr. Fluorine atoms and oxygen atoms were assigned optionally and the minimum *R* value was selected (at approximately 0.3% of the differences). After the least-squares refinements without hydrogen atoms, the *R* index ($= \Sigma||F_o|-|F_c||/\Sigma|F_o|$) was converged at less than 0.03 with anisotropic temperature factors. The position of hydrogen atoms in the structure was determined at the position where residual electron density peaks appeared using the difference Fourier method. Careful examination of the difference Fourier maps indicated two possible hydrogen positions (H1 and H2) near O1 and O2 sites only (Figs. 2.2 and 2.3). These hydrogen atoms were involved but their positions were not parameterized in the least-squares cycles. No significant electron density residue was observed around the fluorine atoms. This finding prompted us to select a model where each $F^-$ and $O^{2-}$ ion is ordered among

four anion sites as shown in Table 2.3. Pudovkina et al. (1973) also determined the values of the structural parameters of prosopite and indicated an ordered distribution of $F^-$ and $O^{2-}$ ions. The chemical structural formula, $Ca_{0.964(2)}Sr_{0.036}Al_2F_4(OH)_4$, obtained from the refinement is approximately consistent with the empirical formula, $(Ca_{0.96}Sr_{0.04})Al_{2.00}F_4[(OH)_{3.72}F_{0.28}]$, obtained from the chemical analysis. The atomic coordinates and anisotropic atomic displacement parameters for prosopite are listed in Table 2.3. The selected interatomic distances are presented in Table 2.4.

**Table 2.2.** Experimental details and crystallographic data of prosopite from Ivigtut, Greenland (sample No. 2)

| | |
|---|---|
| Formula (Sample No. 2: empirical) | $Ca_{0.96}Sr_{0.04}Al_2F_4[(OH)_{3.72}F_{0.28}]$ |
| Formula (refined) | $Ca_{0.964(2)}Sr_{0.036}Al_2F_4(OH)_4$ |
| Space group | *C2/c* |
| *a* (Å) | 6.7103(3) |
| *b* (Å) | 11.1619(5) |
| *c* (Å) | 7.3741(3) |
| *β* (°) | 94.919(2) |
| Radiation used | Mo*K*α |
| Radiation wavelength (Å) | 0.71069 |
| Crystal size (mm) | 0.043×0.048×0.063 |
| Total reflections | 2944 |
| Unique reflections used | 791 |
| Final *R* | 0.0185 |
| Final *wR*2 | 0.0554 |
| GooF | 1.203 |

**(a)**

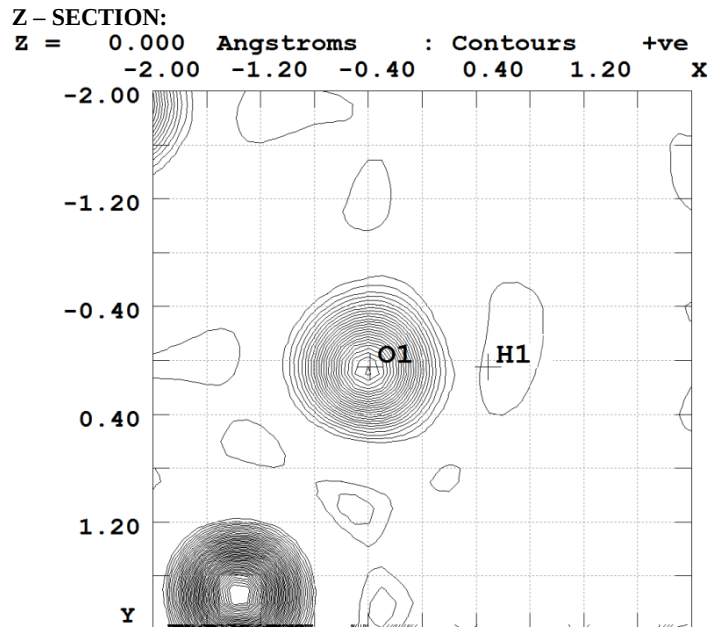


**(b)**

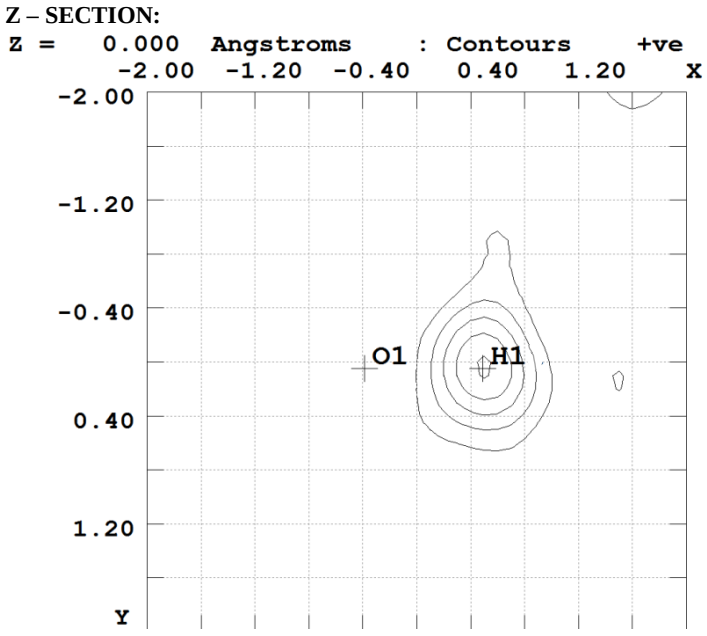


**Figure 2.2.** Position of H1 in the prosopite structure. (a) Fourier map near the O1 site; contours are at an interval of 1.0 e/Å$^3$. (b) Difference Fourier map near the O1 site; contours are at an interval of 0.2 e/Å$^3$.

**(a)**

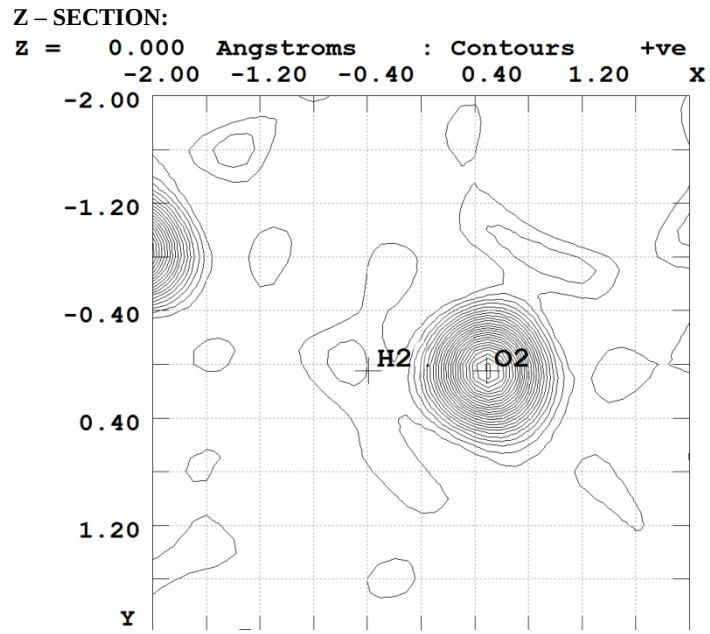


**(b)**

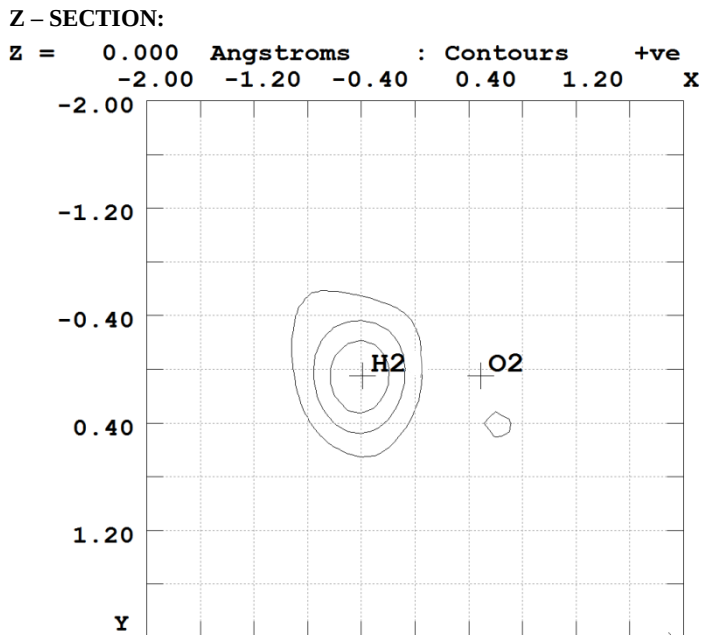


**Figure 2.3.** Position of H2 in the prosopite structure. (a) Fourier map near the O2 site; contours are at an interval of 1.0 e/Å$^3$. (b) Difference Fourier map near the O2 site; contours are at an interval of 0.2 e/Å$^3$.

**Table 2.3.** Atomic coordinates and anisotropic atomic displacement parameters for prosopite from Ivigtut, Greenland (sample No. 2)

| | Occ. | *x* | *y* | *z* | $U_{11}$ | $U_{22}$ | $U_{33}$ | $U_{23}$ | $U_{13}$ | $U_{12}$ |
|---|---|---|---|---|---|---|---|---|---|---|
| Ca | 0.964(2) | 0 | 0.46044(3) | 1/4 | 0.00798(17) | 0.00816(17) | 0.00959(17) | 0 | 0.00281(11) | 0 |
| Sr | 0.036 | 0 | 0.46044(3) | 1/4 | 0.00798(17) | 0.00816(17) | 0.00959(17) | 0 | 0.00281(11) | 0 |
| Al1 | | 1/4 | 1/4 | 0 | 0.0073(3) | 0.0081(3) | 0.0071(3) | 0.00029(19) | 0.0020(2) | -0.00004(19) |
| Al2 | | 0 | 0.14076(5) | 1/4 | 0.0077(3) | 0.0071(3) | 0.0086(3) | 0 | 0.0025(2) | 0 |
| F1 | | 0.07624(12) | 0.38085(7) | 0.96143(11) | 0.0125(4) | 0.0105(4) | 0.0113(4) | 0.0015(3) | 0.0021(3) | 0.0028(3) |
| F2 | | 0.18263(13) | 0.02445(7) | 0.28587(12) | 0.0122(4) | 0.0115(4) | 0.0202(4) | 0.0042(3) | 0.0060(3) | 0.0044(3) |
| O1 | | 0.19954(14) | 0.26342(8) | 0.24864(12) | 0.0074(4) | 0.0108(4) | 0.0072(4) | 0.0003(3) | 0.0002(3) | -0.0014(3) |
| O2 | | 0.02486(14) | 0.15354(8) | 0.99625(12) | 0.0095(4) | 0.0091(4) | 0.0088(4) | -0.0024(3) | 0.0020(3) | -0.0015(3) |
| H1* | | 0.2999 | 0.2661 | 0.3325 | | | | | | |
| H2* | | 0.0338 | 0.0890 | 0.9298 | | | | | | |

* Hydrogen position is not refined.

The maximum peak position in the differential Fourier synthesis was considered as each hydrogen position.

**Table 2.4.** Selected interatomic distances (Å)

| $CaF_6O_2$ dodecahedra | | $Al1F_2O_4$ octahedra | | $Al2F_2O_4$ octahedra | |
|---|---|---|---|---|---|
| Ca-F1[×2] | 2.4012(8) | Al1-F1[×2] | 1.8752(8) | Al2-F2[×2] | 1.7893(9) |
| Ca-F1´[×2] | 2.3863(8) | Al1-O1[×2] | 1.8987(9) | Al2-O1[×2] | 1.9156(10) |
| Ca-F2[×2] | 2.2831(9) | Al1-O2[×2] | 1.8535(9) | Al2-O2[×2] | 1.8982(9) |
| Ca-O1[×2] | 2.5751(10) | | | | |
| Ave. | 2.4114 | | 1.8758 | | 1.8677 |
| Max. | 2.5751 | | 1.8987 | | 1.9156 |
| Min. | 2.2831 | | 1.8535 | | 1.7893 |
| Max.-Min. | 0.2920 | | 0.052 | | 0.1263 |

## 2.3. RESULTS AND DISCUSSION

### 2.3.1. Crystal structure of prosopite

From the chemical analysis, the fluorine content was between 4 and 5 and the quantity of maximum substitution of $F^-$ for $(OH)^-$ in prosopite was estimated to be 25%. This observation may indicate that fluorine content of more than 4 is common in the prosopite structure. As fluorine and oxygen elements have different proton numbers, the attraction between protons and an electron is different (the origin of chemical shift). The ionic radius (1.33 Å for $^{VI}F^-$ and 1.40 Å for $^{VI}O^{2-}$) (Shannon, 1976) and polarizability differ even when they are converted to ions. The atomic scattering factors and Coulombic contribution are also different. The $(OH)^-$ ion with $H^+$ ion and the spherical $F^-$ ion have different anisotropy in chemical bonding. The replacement of $F^-$ in the (OH) sites with large anisotropy is easy. On the contrary, our observation based on both the chemical analysis and structure refinement shows that the substitution of $(OH)^-$ with large anisotropy for F sites with slight anisotropy hardly occurs. H atoms form hydrogen bonds that require bonding directionality and form Coulomb interaction with the surrounding atoms. An appropriate site for hydrogen atom is also required. In our structural observation, no significant H site near F sites was observed. Therefore, we assume the model in which $(OH)^-$ dissolution into F sites does not occur (but the substitution of $F^-$ in OH sites slightly occurs) and propose that the chemical structural formula of prosopite is $CaAl_2F_4[(OH)_{4-x}F_x]$ ($x$ = 0.0–1.0).

The crystal structure of prosopite obtained using the refinement is shown in Figure 2.4.

The fundamental framework structure is identical to that reported by Pudovkina et al. (1973), and the present analysis allows us to demonstrate a model where $F^-$ and $O^{2-}$ anions preferentially reside at each F and O site together with the hydrogen positions bonded to O1 and O2. The crystal structure of prosopite consists of two types of $AlF_2(OH)_4$ octahedra and one kind of $CaF_6(OH)_2$ dodecahedra. The octahedra and dodecahedra form a block unit and large voids are formed between the block units. The voids are filled with hydrogen atoms and are arranged parallel to the [101] direction (Fig. 2.4).

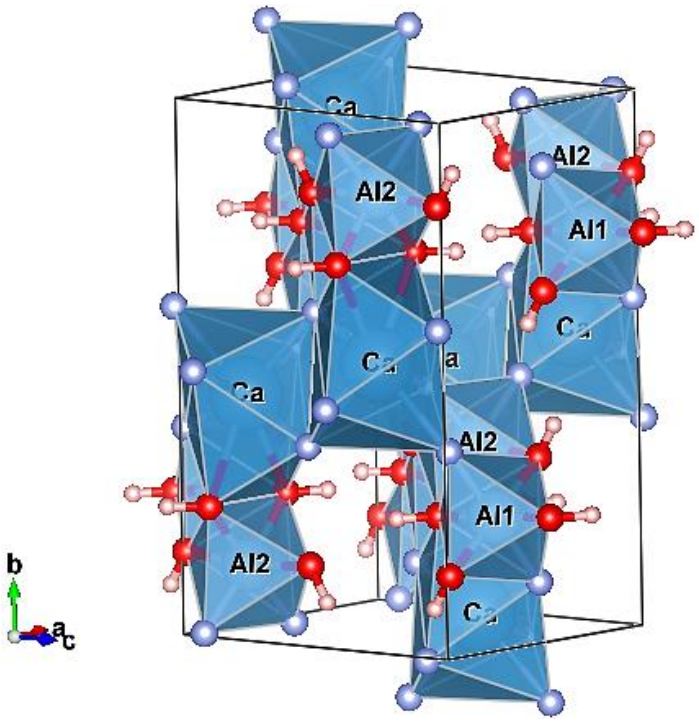


**Figure 2.4.** Crystal structure of prosopite as a perspective view from the direction close to [-101]. The crystal structure was drawn using VESTA (Momma and Izumi, 2011). The tunnels in which hydrogen atoms were located continuously are observed in parallel to [101].

### 2.3.2. Interatomic distances

As $(OH)^-$ has larger ionic radius than $F^-$ for the coordination numbers of four (1.35 Å for $(OH)^-$ and 1.31 Å for $F^-$) and six (1.37 Å for $(OH)^-$ and 1.33 Å for $F^-$) (Shannon, 1976), it can be considered that the interatomic distances of $(OH)^-$ and cations are longer than those of $F^-$ and cations. As shown in Table 2.4, the interatomic distances of Ca-OH (Ca-O1H1) and Al2-OH (Al2-O1H1 and Al2-O2H2) are longer than those of Ca-F and Al2-F in Ca dodecahedra and Al2 octahedra, respectively, and the size difference between the F sites and (OH) sites is apparent. However, such features of Al-F and Al-O distances are not observed in Al1 octahedral sites. The value of 1.8752(8) Å for Al1-F1 is larger than the expected value by Shannon's ionic radii and the Al1-O2 distance is 1.8535(9) Å in the Al1 octahedral site. The tendency of these interatomic distances in this study is similar to that reported by Pudovkina et al. (1973).

### 2.3.3. Bond valence sum calculation and hydrogen bonding

Pudovkina et al. (1973) reported that prosopite structure is characterized by two weak hydrogen bonds O1-H1…O2 and O2-H2…F2 with O1-O2 distance of 2.89 Å and O2-F2 distance of 2.80 Å, respectively. They did not determine the hydrogen positions, but proposed hydrogen bonds from the donor–acceptor anion distances. In order to investigate the electrostatic compensation in prosopite, we also carried out bond valence sum calculations using the method of calculations and parameters given by Brown and

Altermatt (1985). Table 2.5 shows the bond valence sum calculations considering the hydrogen bonding. The O2 and F2 sites act as acceptors in the hydrogen bonds O1-H1…O2 and O2-H2…F2, respectively. The H1…O2 distance is 2.059 Å and the O1-H1…O2 angle is 155.8° (Table 2.6). The H2…F2 distance is 1.977 Å and the O2-H2…F2 angle is 152.7° (Table 2.6). We confirmed the same two hydrogen bonds reported by Pudovkina et al. (1973). They also performed the calculation of the valence balance in the prosopite structure and reported that the valence sum is similar to the formal valence of each atom. As shown in Table 2.5, the estimated crystal structure is appropriate, because the bond valence sum is similar to the ionic valence of each atom. The calculated bond valence sum of 0.860 for F1 is less than the expected value of 1.0. This is due to the long Al1-F1 distance. Similar phenomena were observed in legrandite (Jinnouchi et al., 2016). This phenomenon is caused by the failure to satisfy the local requirement in order to maintain three-dimensional periodicity.

**Table 2.5.** Bond valence sum calculations for prosopite

| | Al1 | Al2 | Ca | Σ(Al,Ca)v | H1 | H2 | Σ(Al,Ca,H)v |
|---|---|---|---|---|---|---|---|
| F1 | 0.410 | | 0.221 | 0.860 | | | 0.860 |
| F1 | | | 0.229 | | | | |
| F2 | | 0.516 | 0.304 | 0.820 | | 0.110 | 0.930 |
| O1 | 0.511 | 0.490 | 0.193 | 1.195 | 0.904 | | 2.099 |
| O2 | 0.579 | 0.513 | | 1.092 | 0.115 | 0.907 | 2.114 |
| Σav | 3.002 | 3.039 | 1.893 | | 1.019 | 1.017 | |

**Table 2.6.** Selected interatomic distances (Å) and angles (°) including hydrogen bonding

| X-H…A | Distance(X-H) (Å) | Distance(X-A) (Å) | Distance (H…A) (Å) | Angle (°) |
|---|---|---|---|---|
| O1-H1…O2 | 0.875 | 2.878 | 2.059 | 155.8 |
| O2-H2…F2 | 0.876 | 2.784 | 1.977 | 152.7 |

# 第 3 章 Chapter 3

# Crystal structure and XANES investigation of petzite, $Ag_3AuTe_2$

# petzite の結晶構造解析と XAFS 分析

## 3.1. INTRODUCTION

Nearly thirty kinds of mineral in which gold is a major component have been confirmed to date, like calaverite $AuTe_2$, sylvanite $(Au,Ag)_2Te_4$, krennerite $(Au,Ag)_2Te_4$, and petzite $Ag_3AuTe_2$, besides native gold. They occur both isolated and in association with other gold minerals. Reports of gold minerals are not infrequent. Gold and silver belong to the coinage metals group in the period table of the elements; they give extensive solid solutions in compounds, including minerals, and also form an alloy, known as electrum. Gold minerals often include heavy pnictogens and chalcogens (Sb, Bi, Se, Te); in particular, several gold and tellurium/antimony compounds are known, with a simple chemical formula, like calaverite and sylvanite, but their crystal structures are far from simple, showing incommensurate modulation under ambient conditions (Schutte & Boer, 1988; Pertlik, 1984; Reithmayer *et al*. 1993; Bindi *et al*., 2009; Bindi & Chapuis, 2017). Even the pure unsubstituted calaverite $AuTe_2$ shows a periodic ordered structure only under high-pressure conditions (Reithmayer *et al*. 1993).

Petzite, $Ag_3AuTe_2$, coexists with coloradoite, HgTe, and hessite, $Ag_2Te$, and occurs as intergrowth with them (Frueh, 1959). Petzite was first synthesized by Thompson (1948) and its structure was determined by Frueh (1959) with a Buerger precession camera from a fragment obtained by fracturing a crystal of hessite in which it occurred as irregular shaped blobs (Frueh, 1959). The crystal structure was later refined by Chamid *et al*. (1978). Thompson (1948, 1949) indicated that petzite is a compound with a definite silver-to-gold ratio, which suggests distinct ordered positions for the silver and gold atoms, corresponding to a three-dimensionally periodic, non-modulated structure, unlike calaverite and sylvanite. Hessite occurs in two polymorphs, the low temperature β phase (space-group type $P2_1/c$) and the high temperature α phase

(space-group type *Fm*3*m*) (Schneider & Schulz, 1993), whereas no polymorphism has been confirmed in either coloradoite (space-group type *F*43*m*) or petzite (space-group type $I4_132$). Frueh (1959) quoted an unpublished thermal analysis showing a transition in petzite at 483 ± 10 K; if confirmed, such a transition would lead to a holohedral polymorph which would make possible a petzite–hessite solid solution at high temperature. Frueh (1959) reported, but did not index, a powder diffractogram at 523 K which differed from that at room temperature; however, microscopic observation showed only a limited shrinking of the crystal, attributed to diffusion of gold in hessite following a higher solubility at high temperature. However, no transformation twinning in heat-treated samples was reported, as one would expect if a phase transition had taken place.

In this study, we have performed a precise structural analysis of petzite crystal samples and clarified the structure details, the site occupancy on each site and bonding character. In addition, Au and Te $L_{III}$-edge XANES measurements have been performed to investigate detailed bonding characteristics such as electrical properties.

## 3.2. EXPERIMENTAL

### 3.2.1. Chemical analyses

Single crystals of petzite $Ag_3AuTe_2$ were obtained from Lake View Mine, Golden Mile, Kalgoorlie, Australia (Kumamoto University, sample reference C133-petzite-single-grain-201532). The sample is brittle, of deep steel grey color and with large single crystals of several millimeters in size. Its chemical composition was determined with a JEOL scanning electron microscope (SEM, JSM-7001F operated at 15 kV, 0.5 mA) equipped with an Oxford energy-dispersive X-ray spectroscope (EDS,

INCA SYSTEM) (Hongu *et al*., 2018). Each pure metal was used as a standard material and the ZAF (atomic number Z, absorption A and fluorescence F) corrections were applied. Measurement points where the total clearly deviated from 100% were excluded. The weight percentages of Au, Ag and Te were 25.25-25.98 wt% Au, 41.55-42.26 wt% Ag and 33.01-34.14 wt% Te. The variation in molar ratio among numerous analytical points with respect to the stoichiometric values was less than a few per cent. Only trace amounts of mercury were detected. Impurities such as arsenic and antimony were below the detection threshold.

### 3.2.2. Single-crystal X-ray diffraction experiments and structure refinements

We have performed single-crystal X-ray diffraction experiments on petzite with a Rigaku R-AXIS RAPID diffractometer (Tokuda *et al*. 2018; Hongu *et al*., 2018). Reflection conditions were consistent with space group $I4_132$. Intensities were measured using graphite-monochromated MoKα (λ = 0.71069 Å) radiation. The data were corrected for Lorentz and polarization factors and for the effect of absorption, which was determined using the integration method based on the observed shape of the specimens. Data reduction results in $R_{int}$ = 0.0968 which, although rather high, is not unusual for a sample containing heavy atoms.

Independent reflections were used for refinement with $I > 3\sigma(I)$ by full matrix-least-squares method. Experimental details are listed in Table 3.1. Refinement calculations were performed using the program *JANA2006* (Petricek *et al*., 2014). The refinement converged smoothly to $R_1$ = 0.0297. An attempt to refine mixed-occupancy Ag/Au on the 8*b* and 24*f* positions did not give any indication of isomorphic substitution, confirming the Ag/Au ordering already reported in previous studies. The

residual peaks (1.74, -1.03 Å $e^{-3}$) are acceptable for a crystal structure containing heavy atoms, considering the difficulties in the absorption correction.

The space group of petzite belongs to a Sohncke type, which means that the structure can occur in two enantiomorphic configurations. The Flack parameter (Flack, 1983) refined to 0.05(3), confirming that the absolute structure is correct. The crystal structure is shown in Figs. 3.1-3.5. The interatomic distances for petzite and the structure refinement data, atomic coordinates and anisotropic atomic displacement parameters are given in Tables 3.2 and 3.3, respectively.

**Table 3.1.** Experimental details for petzite $Ag_3AuTe_2$

| | |
|---|---|
| Crystal data | |
| Chemical formula | $Ag_3AuTe_2$ |
| $M_r$ | 775.8 |
| Crystal system, space group | Cubic, $I4_132$ |
| Temperature (K) | 297 |
| $a$ (Å) | 10.417(8) |
| $V$ (Å$^3$) | 1130.3(15) |
| $Z$ | 8 |
| Radiation type | Mo $K\alpha$ (0.71069 Å) |
| Crystal size (mm) | 0.030×0.047×0.073 |
| $\mu$ (mm$^{-1}$) | 46.076 |
| | |
| Data collection | |
| Diffractometer | Rigaku R-AXIS RAPID |
| Absorption correction | Integration (Busing & Levy, 1957) |
| $T_{min}$, $T_{max}$ | 0.085, 0.251 |
| No. of measured, independent and observed [$I > 3\sigma(I)$] reflections | 2866, 225, 176 |
| $R_{int}$ | 0.0968 |
| $(\sin\theta/\lambda)_{max}$ (Å$^{-1}$) | 0.648 |
| | |
| Refinement | |
| $R[F^2 > 2\sigma(F^2)]$, $wR(F^2)$, $S$ | 0.030, 0.052, 1.04 |
| No. of reflections | 225 |
| No. of parameters | 12 |
| $\Delta\rho_{max}$, $\Delta\rho_{min}$ (e Å$^{-3}$) | 1.74, –1.03 |
| Absolute structure | 71 Friedel pairs used in the refinement |
| Absolute structure parameter | Flack, 0.05(3) |

**Table 3.2.** Interatomic bond distances in petzite

| Atom 1 | Atom 2 | Distance (Å) |
|---|---|---|
| Au | Te | 2.6273(13) |
| Au | Ag | 3.0784(18)×6 |
| Au | Au | 3.6833(3) |
| Ag | Te | 2.9140(18)×3 |
| Ag | Te | 2.9825(19)×3 |
| Ag | Ag | 3.0814(16)×2 |
| Ag | Ag | 3.3053(17)×2 |
| Te | Te | 3.767(3) |

**Table 3.3.** Atomic coordinates and anisotropic atomic displacement parameters for petzite

| | *x* | *y* | *z* | $U_{11}$ | $U_{22}$ | $U_{33}$ | $U_{23}$ | $U_{13}$ | $U_{12}$ |
|---|---|---|---|---|---|---|---|---|---|
| Au (8*b*) | 0.875 | 0.875 | 0.875 | 0.0407(4) | 0.0407(4) | 0.0407(4) | -0.0056(4) | -0.0056(4) | -0.0056(4) |
| Te (16*e*) | 0.22938(8) | 0.22938(8) | 0.22938(8) | 0.0286(4) | 0.0286(4) | 0.0286(4) | -0.0007(4) | -0.0007(4) | -0.0007(4) |
| Ag (24*f*) | -0.13818(15) | 0 | 0.25 | 0.0464(10) | 0.0389(9) | 0.0329(10) | 0 | 0 | 0.0052(7) |

### 3.2.3. X-ray absorption near edge structure (XANES) measurements

The XANES spectra near the Au and Te $L_{III}$-edges were measured in fluorescent mode on beamline BL-9C PF, KEK, Tsukuba, Japan. We also measured several Au and Te minerals for comparison [aurostibite $AuSb_2$ from Krasna Hora, Schoenberg, Czech Republic; calaverite $AuTe_2$ from Lake View Mine, Golden Mile, Kalgoorlie, Australia;

sylvanite $(Ag,Au)Te_2$ from Emperor Mine, Vatukoula, Viti Levu, Fiji; krennerite $Au_3AgTe_8$ from Cripple Creek, Colorado, USA; nagyagite $[Pb_3(Pb,Sb)_3S_6](Au,Te)_3$ from Sacaramb (Nagyag), Transylvania, Romania; and emmonsite $Fe^{3+}{}_2Te^{4+}{}_3O_9 \bullet 2(H_2O)$ from San Miguel Mine, Moctezuma, Sonora, Mexico], all property of Kumamoto University. The synchrotron radiation was monochromated by a Si (111) double-crystal monochromator. X-ray energy calibration was performed by setting the copper metal pre-edge absorption peak to 8978.8 eV. Mirrors were used to eliminate higher harmonics. The measurements were performed using the usual energy resolution to obtain sufficient X-ray flux and for comparison with published results. The details of the measurements are given in the literature (Hiratoko *et al*. 2013; Tobase *et al*. 2018; Yoshiasa *et al*. 2018).

## 3.3. RESULTS AND DISCUSSION

### 3.3.1. Description of the structure and bonding distances in petzite

The crystal structure of petzite was refined by Chamid *et al*. (1978) in the space group $I4_132$, which is a Sohncke type of space group where chiral structures can occur (Nespolo *et al*., 2018). However, no attempt to was made to determine the absolute structure and the structural model essentially coincides with that proposed earlier by Frueh (1959). In this model, the gold atom is coordinated by two tellurium atoms at 2.61 Å and six silver atoms at 3.06 Å; the silver atoms are tetrahedrally surrounded by Te atoms, with two of the Te atoms at 2.92 Å and two at 2.96 Å; the tellurium is coordinated by one gold atom at 2.61 Å, three silver atoms at 2.92 Å and three more silver atoms at 2.96 Å. It was explained that the Au-Te distance is shorter than the Ag-Te distances because there are only two close neighbours for Au in petzite.

Our results support the fully ordered model of petzite, with distinct ordered positions for Au and Ag atoms, proposed in the past by Thompson (1948, 1949), Frueh (1959) and Chamid *et al*. (1978). However, our model corresponds to the opposite handedness with respect to the previous reports. Au was refined on the Wyckoff 8*a* position in the past, but on the 8*b* position in our model. These two positions belong to the same Wyckoff set and are related by the additional generator of the Euclidean normalizer of $I4_132$, which is precisely the inversion through the origin that exchanges the two handednesses. Figures 3.1 and 3.2 show the difference between their model and our model (difference in handedness). At the time of Frueh's (1959) investigation, it was not yet possible to determine an absolute structure. The more recent report by Chamid *et al*. (1978) did not determine the absolute configuration either. The opposite configuration reported previously may therefore have simply been the result of an arbitrary assignment.

The structure of petzite is shown in Figs. 3.3 and 3.4. In the cation-centered description (Fig. 3.3), the structure is based on clusters of six edge-sharing $AgTe_4$ rhombic disphenoids with a common corner, the $AuTe_2$ dumbbell being located in the cavity surrounded by clusters. In the anion-centered description (Fig. 3.4), Te is almost at the center of a triangular face of a monocapped flattened trigonal antiprism $Te[Ag_6Au]$.

Selected interatomic distances are shown in Table 3.2. The Pauling ionic radii of Ag(I), Au(I) and Te(-II) are 1.26, 1.37 and 2.21 Å, respectively. The Shannon radii in sulfides are 0.92 Å for $^{[4]}$Ag(I), 0.58 Å for $^{[2]}$Au(I) and 2.07 Å for $^{[6]}$Te(-II) (Shannon, 1981), whereas covalent radii for Ag, Au and Te are 1.45, 1.36 and 1.38 Å, respectively (Cordero *et al*., 2008).

The rhombic disphenoid around silver has two Ag-Te distances of 2.9140(18) Å and the other two are 2.9825(19) Å; these are slightly shorter than the sum of the Shannon radii for sulfides (2.99 Å) and much shorter than the sum of the ionic radii (3.47 Å) but longer than the sum of the covalent radii (2.83 Å).

The gold atom is coordinated by two tellurium atoms forming a dumbbell with distances of 2.6273(13) Å, which is shorter than the bond distance for either ionic (3.58 Å) or covalent (2.74 Å) bonds, computed as sum of the respective radii, but close to the sum of the Shannon radii for sulfides (2.65 Å). Frueh (1959) explained the shorter linear Au-Te distance with respect to the tetrahedral Ag-Te distances precisely in terms of the lower coordination for gold.

Tellurium is coordinated by one gold atom at 2.6273(13) Å and by six silver atoms, three at 2.9140(18) Å and three more at 2.9825(19) Å. All the seven atoms coordinating the tellurium are on the same side of a geometric plane, and two neighbouring tellurium atoms have their coordinating atoms on opposite sides of this plane, leaving an empty cavity in between (Fig. 3.5). The Te-Te distance [≥ 3.767(3) Å] is far larger than the sum of the covalent radii but shorter than the van der Waals bonding distance (van der Waals radius 1.99 Å; Alvarez, 2013), suggesting the presence of a weak Te-Te bond, which is likely to be responsible for the brittle nature of petzite crystals.

The shortest distances for Ag-Au [3.0784(18) Å] and Ag-Ag [3.0814(16) Å] are very close to each other but somewhat longer than the bond distances in electrum (where Ag and Au are disordered) or metallic silver (~2.88-2.89 Å (Wyckoff, 1963; Venudhar *et al.*, 1978), which suggests the presence of a metallic bond.

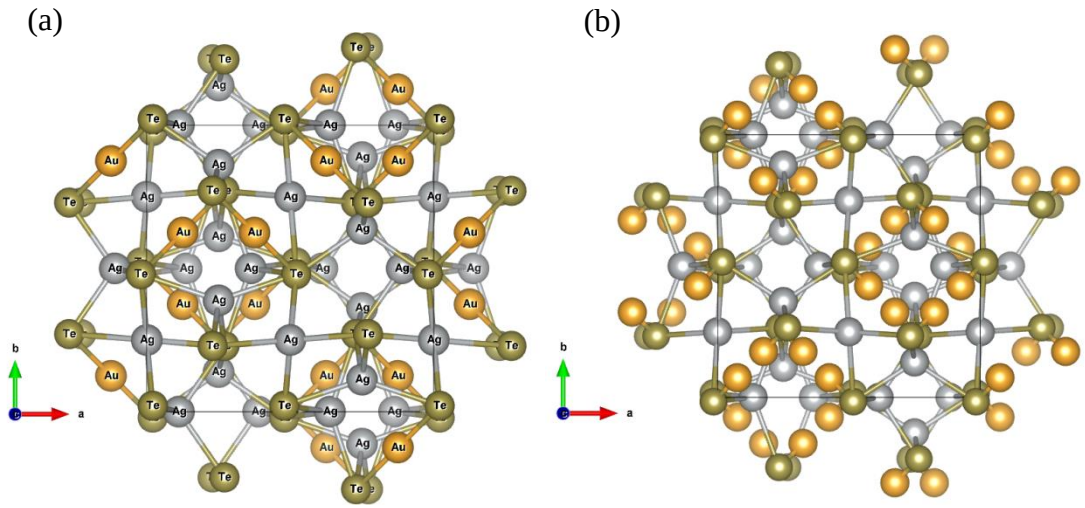


**Figure 3.1.** Crystal structure of petzite projected along the [001] direction. Orange, grey and brown atoms are Au, Ag and Te, respectively. (a) our model; (b) Chamid *et al*. (1978) model. The two models are different in their handedness. Only the Au-Te and Ag-Te bonds are shown.

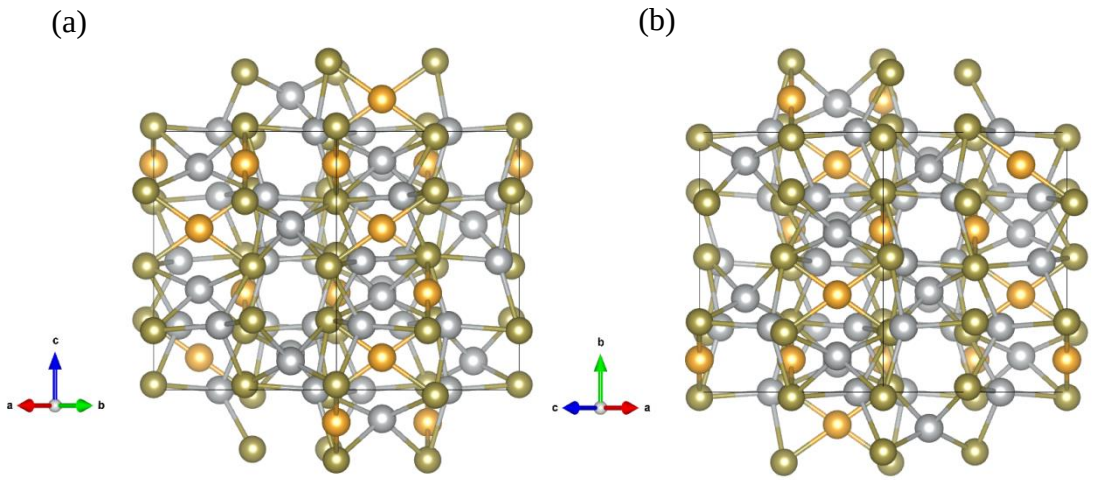


**Figure 3.2.** Crystal structure of petzite projected along the [110] direction. (a) our model; (b) Chamid *et al*. (1978) model. The two models are different in their handedness. Only the Au-Te and Ag-Te bonds are shown.

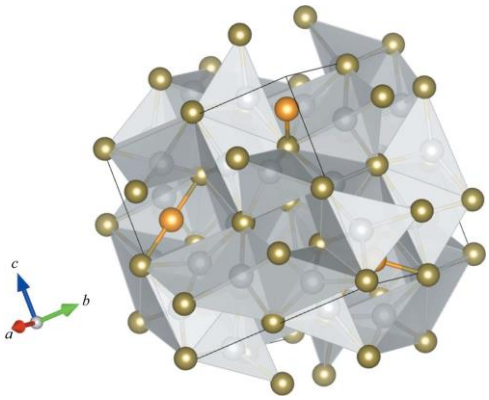


**Figure 3.3.** The cation-centered description of the crystal structure of petzite. In this description, the structure is based on clusters of six edge-sharing $AgTe_4$ rhombic disphenoids with a common corner, the $AuTe_2$ dumbbell being located in the cavity surrounded by clusters. Figure drawn with VESTA (Momma & Izumi, 2011).

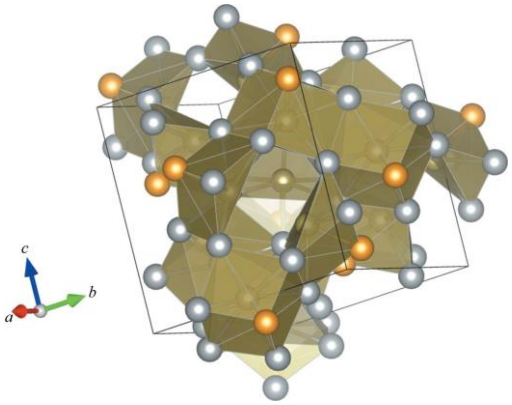


**Figure 3.4.** The anion-centered description of the crystal structure of petzite. In this description, tellurium is almost at the center of a triangular face of a monocapped flattened trigonal antiprism $Te[Ag_6Au]$. Figure drawn with VESTA.

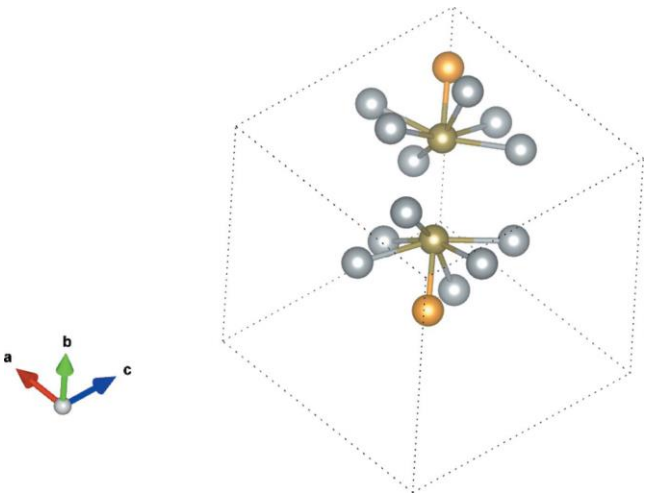


**Figure 3.5.** A portion of the crystal structure of petzite, showing the region around two neighbouring tellurium atoms. The silver and gold atoms coordinated to the same tellurium atom are all on the same side of a geometric plane, and two neighbouring tellurium atoms have their coordinating atoms on opposite sides of this plane, leaving an empty cavity in between, suggesting the presence of a weak Te-Te bond. Figure drawn with VESTA.

### 3.3.2. Temperature factor and estimated Debye temperature $\theta_D$

The anisotropic atomic displacement parameter for each atom in petzite is shown in Table 3.3. The temperature factor at each site in the petzite structure increases in the order of Te, Ag and Au sites. The Au atom in petzite has the largest amplitude of

thermal vibration, Which results from the covalent Te-Au-Te linear bond. The atomic displacement parameter relates to the mass of the atom.

Debye temperature, $\theta_D$, is one of the indices of a physical quantity by which comparison is possible. The Debye temperature $\theta_D$ correlates with physical properties such as the hardness of crystals. The value $\theta_D$ for each atom can be estimated using the dynamic component in the Debye-Waller factor based on the Debye approximation (Willis & Pryor, 1975; Wood *et al*., 2002; Christensen *et al*., 2006; Nakatsuka *et al*., 2011; Yoshiasa *et al*., 2016). We have estimated $\theta_D$ for each atom using the values of *U* (Table 3.3) under the assumption of no static disorder components of atoms. We obtained $\theta_D$ values for Au, Ag and Te in petzite of 73.3, 101.1 and 108.5 K, respectively. These are significantly lower than the corresponding values in the pure metals (178, 221 and 152 K, respectively), reflecting the different binding forces in the telluride with respect to the respective metals.

### 3.3.3. Au and Te $L_{III}$-edge XANES spectra and bonding character in petzite

Many gold minerals and compounds are represented by simple chemical formulae and adopt basic structures. Aurostibite, calaverite and sylvanite have structures related to pyrite- and $CdI_2$-type structures. Compounds with gold and group V or group VI elements have semi-metallic properties. In the case of pyrite- and $CdI_2$- type compounds, the bonding property among the group V or VI elements affects the main electrical properties. Petzite, $Ag_3AuTe_2$, contains more gold and silver than calaverite and sylvanite, and the metallic character of the bonding between gold and silver is recognized. On the other hand, Te-Te distances do not support the existence of electron sharing among the tellurium atoms but only a weak interaction of van der Waals type.

On the high-energy side of the absorption edge in Au $L_{III}$-edge XANES spectrum, a strong first peak (white line) appears due to electron transfer from the Au atoms to the anions. This peak makes it possible to compare electron polarization, ionic and metallic character for Au atoms. Figure 3.6 shows the Au $L_{III}$-edge XANES spectra for petzite and reference Au minerals. The shape of the XANES spectrum for petzite clearly resembles that of metallic gold, thus the chemical bonding of gold in petzite has a more pronounced metallic character than in other gold minerals.

Figures 3.7(a) and 3.7(b) show the Te $L_{III}$-edge XANES spectra and their first-derivative curves for petzite and reference Te minerals. Emmonsite, $Fe^{3+}{}_2Te^{4+}{}_3O_9 \bullet 2(H_2O)$, is a tellurium salt with a transparent greenish yellow color. Tellurium in this mineral is a tetravalent cation. The absorption edge of cation-leaving electrons shifts to the higher energy side than that of the metal. Conversely, the absorption edge of the anion-obtained electrons shifts to the lower energy side. A chemical shift of the threshold energy at absorption edge occurs in response to the change in the valence state, and the threshold energy shifts to the lower energy side due to the increase in valence of the anion. The Te $L_{III}$-edge absorption edge for petzite is located on the lowest energy side among these minerals, and partial electron transfer to Te atoms is recognized.

The maximum value of the first derivative [Fig. 3.7(b)] represents the position of the maximum gradient in the XANES spectrum showing the threshold energy of the absorption edge (Okudera *et al*. 2012). When comparing peak intensities and positions in the first derivative of the XANES spectrum [Figure 3.7(b)], the first peak on the lowest energy side has the same height as the second peak for Te in petzite and the second peak is nearly the same energy position as the main peaks in calaverite and

nagyagite, $Pb_5Au(Te,Sb)_4S_{5-8}$, a rare sulfide mineral which occurs in association with gold ores. Therefore, it can be concluded that the bonding of Te in petzite has a partial ionic character and the valence state is intermediate between metallic and anionic. In particular, the supply of electrons from Au and Ag seems evident. This is consistent with the Te-Te distance [≥ 3.767(3) Å], which is considerably longer than those in calaverite [2.871(6) Å; Pertlik, 1984] and sylvanite (2.88 Å; Tunell, 1941), as should be expected from the covalent character of the Te-Te bonding in the latter sulfides.

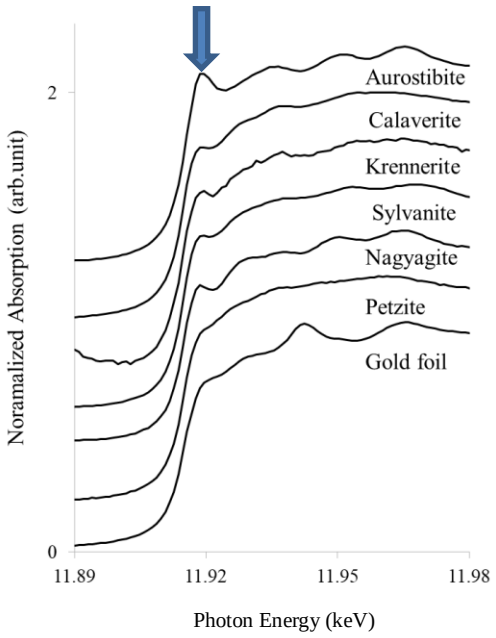


**Figure 3.6.** Au $L_{III}$-edge XANES spectra for petzite and reference Au minerals. The arrow indicates the white line at the absorption edges.

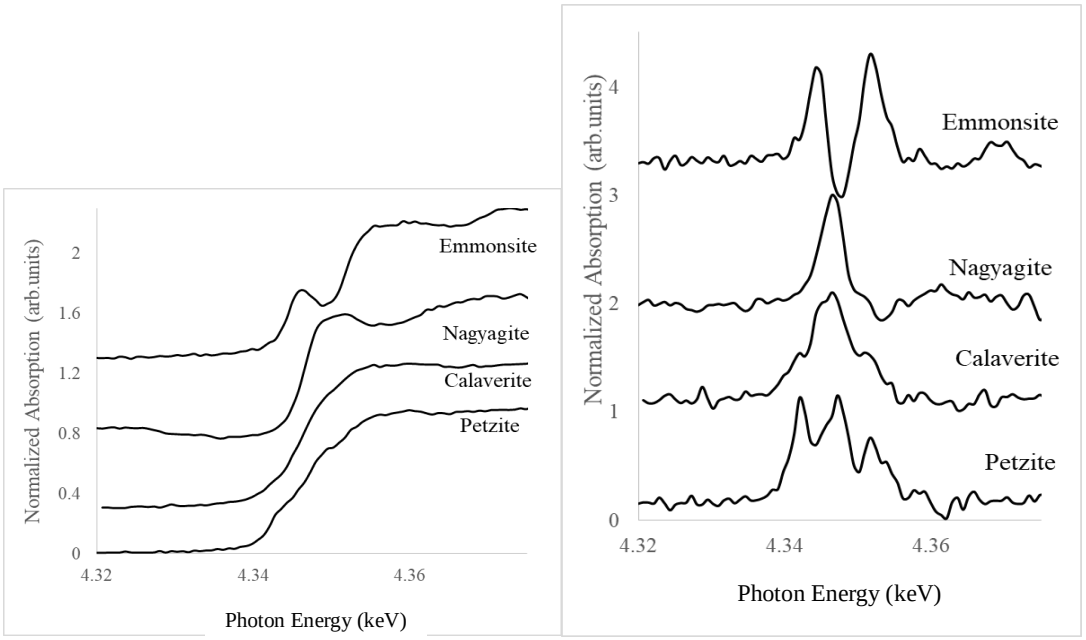


(a) (b)

**Figure 3.7.** (a) Te $L_{III}$-edge XANES spectra of petzite and reference tellurium compound minerals. (b) First derivatives of the Te $L_{III}$-edge XANES spectra of petzite and reference tellurium compound minerals.

### 3.4. CONCLUSIONS

Petzite has an ideal stoichiometric chemical composition. Impurities such as arsenic and antimony were not detected in our sample. Our structure refinement essentially confirms previous reports, but the absolute structure is actually the opposite with respect to the model. The fact that no attempt to determine the absolute structure was reported in the past casts some doubt on the correctness of the previous reports, unless the opposite enantiomorph was indeed found. Should that be the case, the question of the possible relation between the formation environment and the handedness of the structure naturally arises.

The chemical bonding of Au in petzite has a more pronounced metallic character than that in other gold minerals. The Te $L_{III}$-edge XANES spectrum in petzite has its absorption edge at the lowest energy among the gold tellurides and partial electron transfer to Te atoms is recognized. The Te bonding in petzite shows a partially ionic character and the valence state is intermediate between metallic and anionic. Interatomic distances for Ag-Te in petzite can be interpreted as presenting some ionic contribution to the otherwise covalent nature of the bond. A weak Te-Te bond is suggested both by the interatomic distance, which is shorter than the van der Waals bonding distance, and the geometry of the Te-Au/Ag coordination, and it is likely to be responsible for the brittle nature of petzite crystals.

# 第 4 章 Chapter 4

# XAFS study of Sb and As in Cretaceous-Tertiary boundary sediments

# 白亜紀-第三紀境界堆積物中の Sb, As の XAFS 解析

## 4.1. INTRODUCTION

After unusually high concentrations of Ir in the Cretaceous-Tertiary (K-T) boundary sediments were found by Alvarez et al. (1980), an asteroid impact was considered to have caused the K-T mass extinction. These Ir-rich K-T boundary sediments, recently named Cretaceous-Paleogene (K-Pg) boundary sediments, are found throughout the world (e.g., Stevns Klint in Denmark, Gubbio in Italy, Caravaca in Spain, and Woodside Creek in New Zealand). In addition to Pt-group elements such as Ir, the boundary sediments are also enriched with lithophile element Cr, siderophile elements such as Co and Ni, and chalcophile elements such as Cu, Zn, As, and Sb (Strong et al., 1987; Schmitz, 1992). These boundary sediments also include the markers for asteroid impact, such as some shocked quartz grains, tektites, and spherules. The high contents of Cr and Ni in the boundary sediments are considered to be mainly derived from asteroid material, and the concentrations of Cu, Zn, As, and Sb are considered to be derived from the impact ejecta from terrestrial sources (Strong et al., 1987; Schmitz, 1992). Concerning the origins and concentration processes of elements such as Zn, As, and Sb, studies related to volcanism (Officer and Drake, 1985), and precipitation from seawater (Gilmour and Anders, 1989; Schmitz, 1992) have been reported.

In particular, concentrations of Sb and As are unusually high. Gilmour and Anders (1989) reported that bulk K-T boundary sediments had Sb contents of 0.9-9.4 ppm and As contents of 7.2-256 ppm. The Sb and As contents in K-T boundary sediments are concentrations of 10-100 times higher than the average contents in the Earth's crust. However, the origins, concentration processes, and the geochemical and environmental behaviors of Sb are not well known. Sakai et al. (2007) and Okube et al. (2012) clarified

the local structures around As and Zn atoms in K-T boundary sediments from Stevns Klint using XAFS analyses. They proposed that As occupies the tetrahedral $AsO_4$ site in ferrihydrite and Zn occupies the tetrahedral $ZnO_4$ site in a willemite-like framework structure. Okube et al. (2012) also proposed that precipitation of Zn took place under high pH conditions, such as in seawater. Furthermore, Miyano et al. (2016) determined the local structures of Ca, Cr, Mn, Fe, and Ni atoms in K-T boundary sediments and clarified the effects of weathering, diagenesis, and life activity under the sedimentation. Tobase et al. (2015) reported that the local structures of Zr in K-T sediments maintain a glass structure and keep the thermal quenching records by the asteroid impact in the Zr XAFS study in K-T boundary sediments. The samples and XAFS measurement points of K-T boundary sediments used in Sakai et al. (2007), Okube et al. (2012), Miyano et al. (2016), and Tobase et al. (2015) were the same as those used in this study. In this study, we similarly determined the local structure around Sb atoms to obtain information about the chemical state and coordination environment of Sb atoms in K-T boundary sediments by Sb K-edge XAFS spectroscopy. Additionally, we performed As K-edge XAFS measurements of the same group 15 elements as Sb in the periodic table. This XAFS study may provide information about asteroid impact and the consequential soiling of the global environment by falling dust and ashes.

## 4.2. SAMPLES AND EXPERIMENTAL METHODS

Our sample of K-T boundary sediments was obtained from Stevns Klint in Denmark (Sakai et al., 2007; Okube et al., 2012). The K-T boundary sediments of Stevns Klint are well known as marine K-T boundary layers. Here, we analyzed the reddish brown

sediments located in the lower part of the K-T boundary sediments (Fig. 4.1). The Sb and As contents in the reddish brown sediment were reported as 14 ppm and 120 ppm, respectively (Schmitz, 1985). We also confirmed the approximate content of Sb and As in the sediment sample using XAFS measurements. X-ray diffraction (XRD) and microscopic observation showed that the crystalline part of the reddish brown sediment mainly consisted of smectite, spherules, and goethite (e.g., Schmitz, 1985; Drits et al., 2004). In this study, X-ray powder diffraction analysis was performed to identify the constituent crystalline minerals in the analyzed sample. The sample contained smectite (montmorillonite), calcite, and small amounts of quartz and goethite. A glass component was not observed in the spherules. Ca and Fe were the main constituent elements. The Ca and Fe crystalline phases in K-T boundary sediments were mainly calcite and goethite. A quantitative estimation of non- and low crystalline phases in the sample cannot be performed using XRD. Using XAFS analyses, Miyano et al. (2016) reported that the Ca local structure shows diopside-like structure and the Fe local structure is midway between goethite and hematite in the same of K-T boundary sediments from Stevns Klint. In the iron oxide phases, low crystalline ferrihydrite (schwertmannite) was also observed by XAFS experiment in the same sample used in this study (Sakai et al., 2007). Therefore, the main phases of Ca and Fe in K-T boundary sediments sample obtained by XAFS and XRD methods differ. This strongly suggests that information about the non- and low crystalline phases may be obtained by the XAFS method. In this study, the sample used for the XAFS measurements did not contain spherules. To investigate the local structure around Sb atoms in K-T boundary sediments, we prepared several references of natural Sb minerals, such as stibnite ($Sb_2S_3$), getchellite ($AsSbS_3$), ullmannite (NiSbS), cylindrite ($Pb_3Sn_4FeSb_2S_{14}$), swedenborgite ($NaBe_4SbO_7$), welshite

[$Ca_4Mg_9Sb_3O_4(Si_6Be_3AlFe_2O_{36})$], and romeite [$(Ca,Fe,Mn,Na)_2(Sb,Ti)_2O_6(O,OH,F)$], soils containing ferrihydrite (schwertmannite) near Sb and As mines, and Sb compounds, such as $Sb_2O_3$ and $Sb_2O_5$. Samples for soils containing ferrihydrite (schwertmannite) were collected from Ichinokawa antimony mine, Ehime, Japan, and Shimonita (Nishinomaki) arsenic mine, Gunma, Japan. The ferrihydrite (schwertmannite) soil sample from the drainage of Shimonita (Nishinomaki) As mine adsorbs As(V) as arsenate ion (Fukushi et al., 2003a). To study the local structure around As atoms in K-T boundary sediments, we prepared four reference natural As minerals as used in Sakai et al. (2007) : erythrite [$Co_3(AsO_4)_2•8H_2O$], legrandite [$Zn_2AsO_4(OH)•H_2O$], conichalcite [$CaCuAsO_4(OH)$], ferrihydrite (schwertmannite) (from Horobetsu mine, Hokkaido, Japan), and two reference soil samples containing ferrihydrite (schwertmannite) near Ichinokawa Sb mine (Keyakidani and Noboritate). The ferrihydrite from Horobetsu mine strongly sorbs As (+5) as the arsenate $(AsO_4)^{3-}$ (Sakai et al., 2007). Sb and As K-edge XAFS measurements were performed with a Si (311) double crystal monochromator at the BL-NW10A beamline of the Photon Factory in the High Energy Accelerator Research Organization (KEK), Tsukuba, Japan. The spectra near the Sb and As K-edge were collected in transmission and fluorescence modes using a Lytle-type detector. The XAFS measurements were performed in a non-destructive state without the treatment of the analyzed samples. Analyses of XAFS data were performed using XAFS93 and MBF93 programs (Maeda, 1987; Yoshiasa et al., 1999). The radial structural function (RSF) was obtained by the Fourier transform over the *k* range of $2.5 < k < 9.0$ Å$^{-1}$ for the K-T boundary sediments sample. In the quantitative analysis for the K-T boundary sediments sample, stibnite, swedenborgite, welshite, romeite, and ferrihydrite (schwertmannite) soil samples, $Sb_2O_3$ and $Sb_2O_5$, we used the Fourier

filtering technique and a nonlinear least-squares structural parameters fitting method with an analytical extended X-ray absorption fine structure (EXAFS) formula (Maeda, 1987; Yoshiasa et al., 1999).

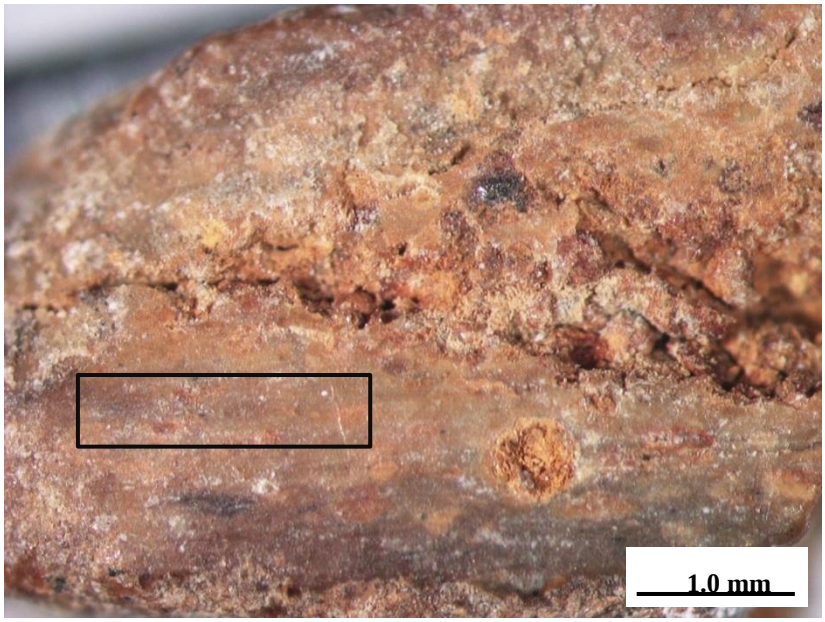


**Figure 4.1.** Photograph of the reddish brown sediment in K-T boundary sediments. Width of the photograph is 5.0 mm. The analyzed point is outlined by the black border.

## 4.3. RESULTS

### 4.3.1. Sb and As K-edge XANES spectra of reference materials and K-T boundary sediments

The XANES spectra of Sb in K-T boundary sediments, various kinds of reference Sb

minerals, soils containing ferrihydrite (schwertmannite), and $Sb_2O_3$ and $Sb_2O_5$ are shown in Figure 4.2. The threshold energies (defined as the maximum of differentiation of XANES spectrum) are listed in Table 4.1. The threshold energy of K-T boundary sediments is 30.4489 keV. The threshold energy of K-T boundary sediments is 2.6-8.5 eV higher than those of Sb sulfide minerals, such as stibnite, getchellite, ullmannite and cylindrite, and $Sb_2O_3$, and the XANES pattern also differ from those of Sb sulfide minerals and $Sb_2O_3$. The XANES pattern and the threshold energy of K-T boundary sediments are similar to those of two ferrihydrite (schwertmannite) soil samples. The threshold and main peak-top energies for K-T boundary sediments are similar to those for swedenborgite and $Sb_2O_5$, and there is no chemical shift in the threshold energies among K-T boundary sediments, $Sb^{5+}$ oxide complex minerals (such as swedenborgite, welshite, and romeite), and $Sb_2O_5$. As shown in Figure 4.2 and Table 4.1, the oxidation state of Sb in K-T boundary sediments is estimated to be $Sb^{5+}$. Sb is coordinated with oxide ions and exists in the same local structural position as Sb in ferrihydrite (schwertmannite).

The XANES spectra of As in K-T boundary sediments and reference materials are shown in Figure 4.3. The threshold energies are listed in Table 4.2. The threshold energy of K-T boundary sediments is 11.8695 keV. The threshold energy of K-T boundary sediments is approximately similar to those of $As^{5+}$ minerals, such as erythrite, legrandite, and conichalcite. The XANES pattern of K-T boundary sediments is similar to those of three ferrihydrite (schwertmannite) soil samples. The oxidation state of As of K-T boundary sediments is estimated to be $As^{5+}$ and As is coordinated as arsenate ion in ferrihydrite (schwertmannite) (Fig. 4.3 and Table 4.2). This result is the same as that reported previously by Sakai et al. (2007). Sb and As in K-T boundary sediments are

coordinated with oxide ions, and Sb and As exist in the same local structure positions as Sb and As in ferrihydrite (schwertmannite).

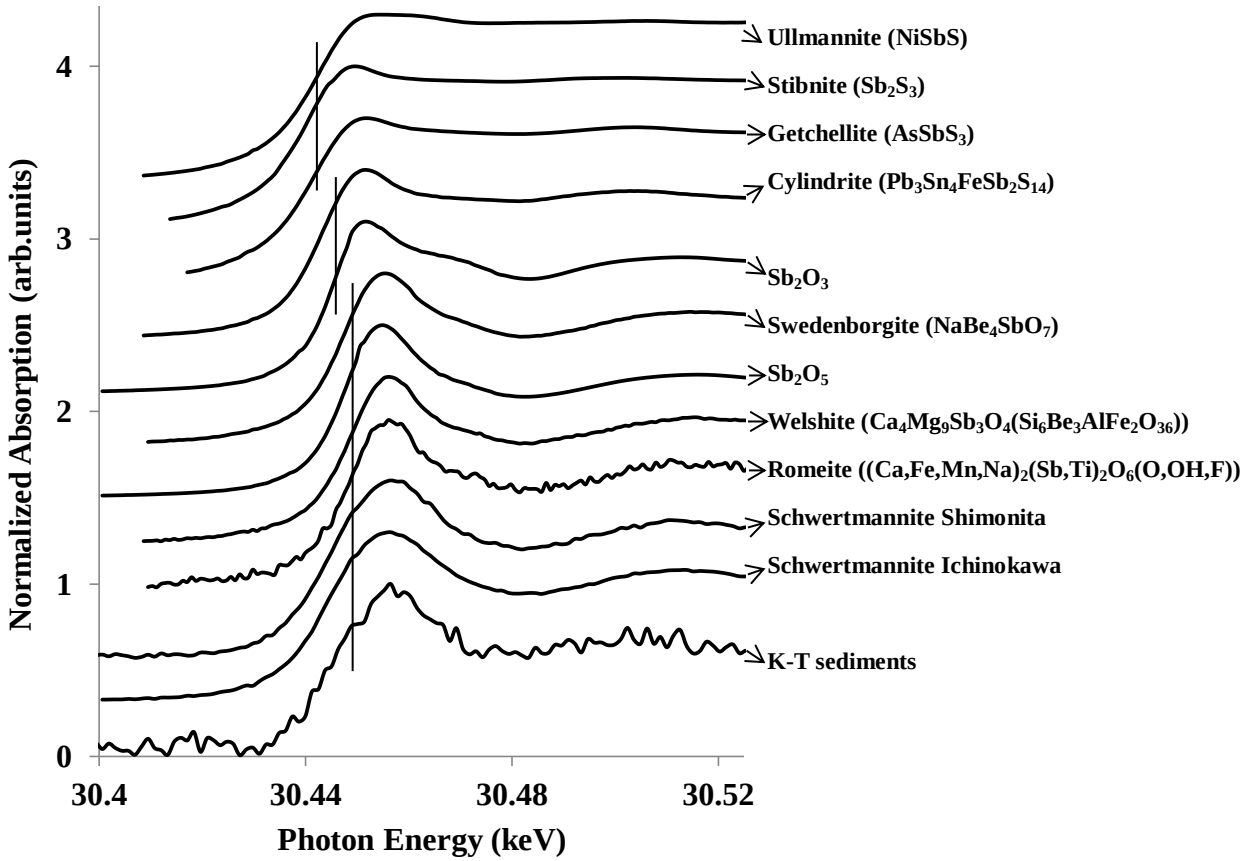


**Figure 4.2.** Sb K-edge XANES spectra of K-T sediments, reference antimony minerals, ferrihydrite (schwertmannite) soil samples, $Sb_2O_3$ and $Sb_2O_5$. The threshold energies are shown by three solid lines.

**Table 4.1.** The threshold energies of Sb K-edge XANES spectra

| Sample | Threshold photon energy (keV) |
|---|---|
| Ullmannite | 30.4424 |
| Stibnite | 30.4404 |
| Getchellite | 30.4425 |
| Cylindrite | 30.4442 |
| $Sb_2O_3$ | 30.4463 |
| Swedenborgite | 30.4493 |
| $Sb_2O_5$ | 30.4506 |
| Welshite | 30.4501 |
| Romeite | 30.4501 |
| Schwertmannite Shimonita | 30.4489 |
| Schwertmannite Ichinokawa | 30.4489 |
| K-T sediments | 30.4489 |

The resolution of photon energy is 0.1 eV.

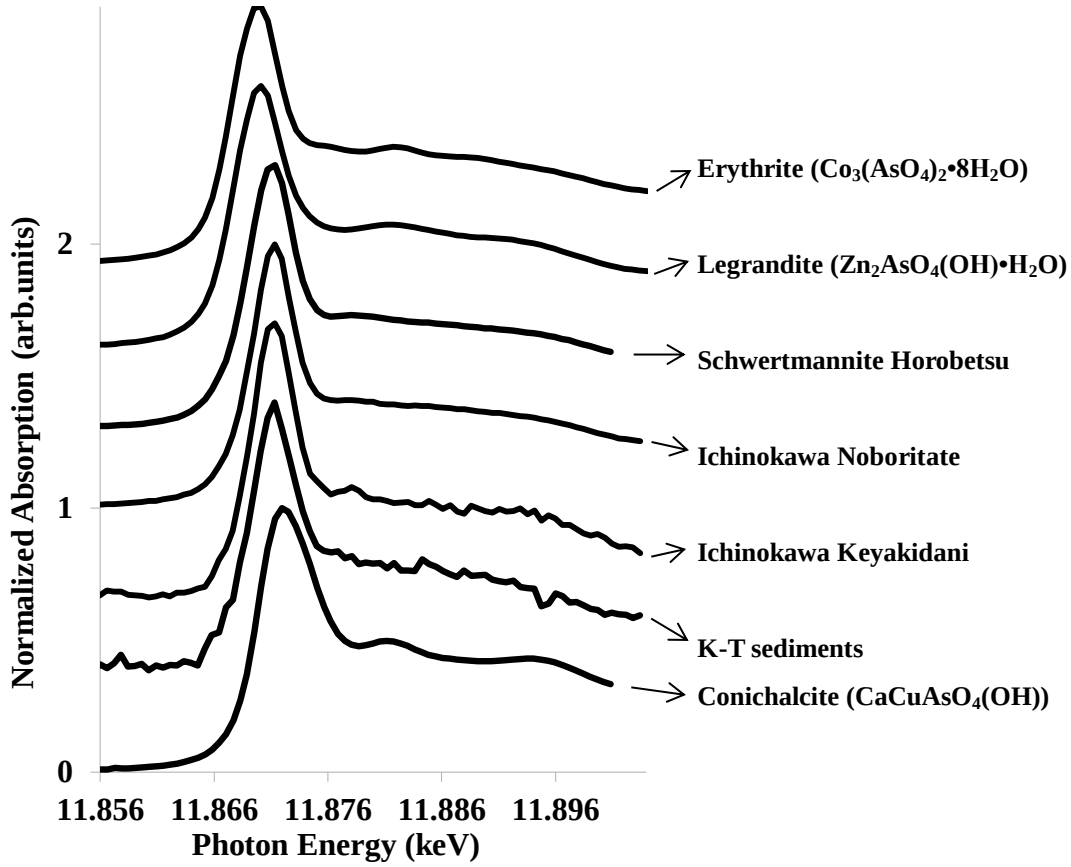


**Figure 4.3.** As K-edge XANES spectra of K-T sediments, reference arsenic minerals and ferrihydrite (schwertmannite) soil samples.

**Table 4.2.** The threshold energies of As K-edge XANES spectra

| Sample | Threshold photon energy (keV) |
|---|---|
| Erythrite | 11.8677 |
| Legrandite | 11.8677 |
| Schwertmannite Horobetsu | 11.8689 |
| Ichinokawa Noboritate | 11.8695 |
| Ichinokawa Keyakidani | 11.8695 |
| K-T sediments | 11.8695 |
| Conichalcite | 11.8701 |

The resolution of photon energy is 0.1 eV.

### 4.3.2. Radial structure function and local structure

The EXAFS $k^3\chi(k)$ functions were transformed into RSFs for Sb K-edge of eight reference materials and K-T boundary sediments, as shown in Figure 4.4. To obtain further information on the structure parameters, we performed the parameter fitting with analytical EXAFS formulae. The obtained structural parameters are summarized in Table 4.3. The Sb-O interatomic distance in K-T boundary sediments sample is 1.99(1) Å. The distance is comparable with the octahedral $Sb^{5+}$ (0.60 Å) and $O^{2-}$ (1.40 Å) ionic radii by Shannon (1976). The Sb-O interatomic distance in the K-T boundary sediments sample is similar to those in two ferrihydrite (schwertmannite) samples (1.98(1) Å), welshite (2.01(2) Å), swedenborgite (1.98(2) Å), and $Sb_2O_5$ (1.98(1) Å). The RSF for K-T boundary sediments is similar in shape to the compound with $Sb^{5+}O_6$ coordination

sites. Since $Sb^{3+}$ with a large ionic radius occupies a three–fold coordinated site, the $Sb^{3+}$-O distance is 1.98(1) Å in $Sb_2O_3$. The XANES spectra and RSF for Sb atoms showed that Sb in K-T boundary sediments has a high oxidation state $Sb^{5+}$ and is stored in the $SbO_6$ octahedral coordination environment. Sb in K-T boundary sediments is considered to be incorporated in ferrihydrite (schwertmannite) from XANES and EXAFS analyses.

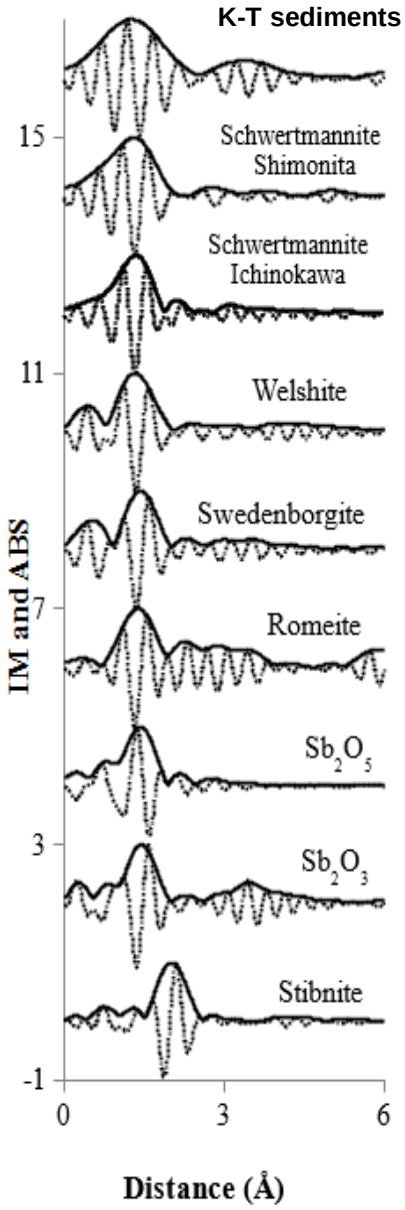


**Figure 4.4.** Fourier transforms of the Sb K-edge EXAFS oscillation function for reference materials and K-T sediments. No EXAFS phase shift corrections are made.

**Table 4.3.** The structure parameters determined by EXAFS and diffraction methods

| Sample | Sb-O distance by EXAFS (Å) | Sb-O distance by diffraction (Å) | Coordination number |
|---|---|---|---|
| K-T boundary sediments | 1.99(1) | — | 6 |
| Schwertmannite Shimonita | 1.98(1) | — | 6 |
| Schwertmannite Ichinokawa | 1.98(1) | — | 6 |
| Welshite | 2.01(2) | 1.982-1.991 (Grew et al., 2007) | 6 |
| Swedenborgite | 1.98(2) | 1.97 (Huminicki and Hawthorne, 2001) | 6 |
| Romeite | 1.97(1) | 1.97 (Zedlitz, 1932) | 6 |
| $Sb_2O_3$ | 1.98(1) | 1.98 | 3 |
| $Sb_2O_5$ | 1.98(1) | 1.99 | 6 |
| Sample | Sb-S distance by EXAFS (Å) | Sb-S distance by diffraction (Å) | Coordination number |
| Stibnite ($Sb_2S_3$) | 2.52(3) | 2.53 | 3 |

The Sb-O interatomic distances in romeite, swedenborgite and welshite are determined using X-ray diffraction method by Zedlitz (1932), Huminicki and Hawthorne (2001), and Grew et al. (2007), respectively.

## 4.4. DISCUSSION

Antimony is a rare metal element widely distributed in the lithosphere and mainly associated with arsenic as a sulfide or oxide. Sb sulfide minerals such as stibnite generally occur in hydrothermal deposits. Swedenborgite and welshite have been found only in the Långban deposit in Sweden, where they are the constituent of skarns (Huminicki and Hawthorne, 2001; Grew et al., 2007). In general, the natural abundance of Sb in soil and freshwater is low (Filella et al., 2002). However, high concentrations of Sb in both soil and water can be found near Sb mines and in areas contaminated by human activities. Sb belongs to group 15 in the periodic table below As, and $Sb^{3+}$ and $Sb^{5+}$ are the most frequently observed species in the environment. It is known that $Sb^{5+}$ is stable form in soil and soil water under an equilibrium situation within the Earth's surface environment (Mitsunobu et al., 2006). The behavior of Sb is not well known in comparison with that of As (Wilson et al., 2010), and few studies have clarified the correlation between Sb and As few studies have clarified the correlation between Sb and As . For example, Vink (1996) reported that the solubility and complex ion behaviors of $Sb^{5+}$ with the $Sb^{5+}(OH)_6^-$ oxyanionic form resemble those of $HAsO_4^{2-}$ and $H_2AsO_4^-$. The chemical behavior of $Sb^{5+}$ is presumed to be similar to that of $As^{5+}$, but the relationship between $Sb^{5+}$ and $As^{5+}$ may not always be established. A close correlation of coprecipitation was observed between As and Fe (Ebihara and Miura, 1996; Sakai et al., 2007). Sakai et al. (2007) also proposed that As in K-T boundary sediments has a high oxidation state $As^{5+}$ and As ion coprecipitated with Fe ion as ferrihydrite. We propose that Sb correlates closely with As ion and also coprecipitated with As and Fe ions. XAFS analyses (Mitsunobu et al., 2006) have clarified that the host phases of Sb and As in soil samples of the Sb mine tailing and in laboratory soil-water systems are Fe(III)

hydroxide. In the metastable phase, poorly crystalline ferrihydrite is known to transfer into crystalline goethite and/or hematite with aging in an oxidation environment. Using Sb EXAFS analyses, Mitsunobu et al. (2010, 2013) reported in detail that $Sb^{5+}$ in the solid phase is structurally incorporated into crystalline goethite and/or hematite generated by the ferrihydrite transformation. Experiments have also shown that the transformation of schwertmannite to goethite may be retarded by the presence of absorbed As(V) in the structure (Fukushi et al., 2003b). High concentrations of Sb and As in K-T boundary sediments are considered to not originate from Sb and As mines and/or human activities. However, considering that Sb and As in K-T boundary sediments are high oxidation states ($Sb^{5+}$ and $As^{5+}$) and the existence of ferric hydroxides in K-T boundary sediments, the environment at K-T boundary sediments resembles that of soil contaminated by Sb and As in local areas at the present time. Therefore, Sb and As in K-T boundary sediments are suggested to be incorporated in low crystalline ferrihydrite (schwertmannite) through precipitation and diagenesis caused by sedimentation.

Abundant ferric hydroxides [e.g., ferrihydrite (schwertmannite) and goethite] occur in the sediment generated by the effect of the asteroid and/or impact ejecta that contain many Fe ions compared with the surrounding geological materials. Although it was a short period of time after the asteroid impact, one of the causes of unusually high concentrations of Sb and As in K-T boundary sediments is considered to be due to the fall and deposition of large amounts of dust from the impact ejecta to the Earth's surface, along with Fe ions contained in the asteroid and/or impact ejecta. The concentration processes of Sb and As into K-T boundary sediments after the asteroid impact are schematically shown in Figure 4.5. Unusual concentrations of Sb and As on a global

scale does not occur under the usual sedimentation environment. It is considered that the sudden increase of Fe, As, and Sb contents have resulted from the increase in impact ejecta on a global scale and precipitation by oxidation of these ions causes unusual concentrations. The existence of abundant Fe leads to concentration by coprecipitation of Sb and As from the environment. In an unusual environment, such as K-T boundary sediments, the unusually high concentrations of $Sb^{5+}$ and $As^{5+}$ could become an index for the degree to which the global environment was soiled with dust and ashes derived from asteroid material and/or impact ejecta falls.

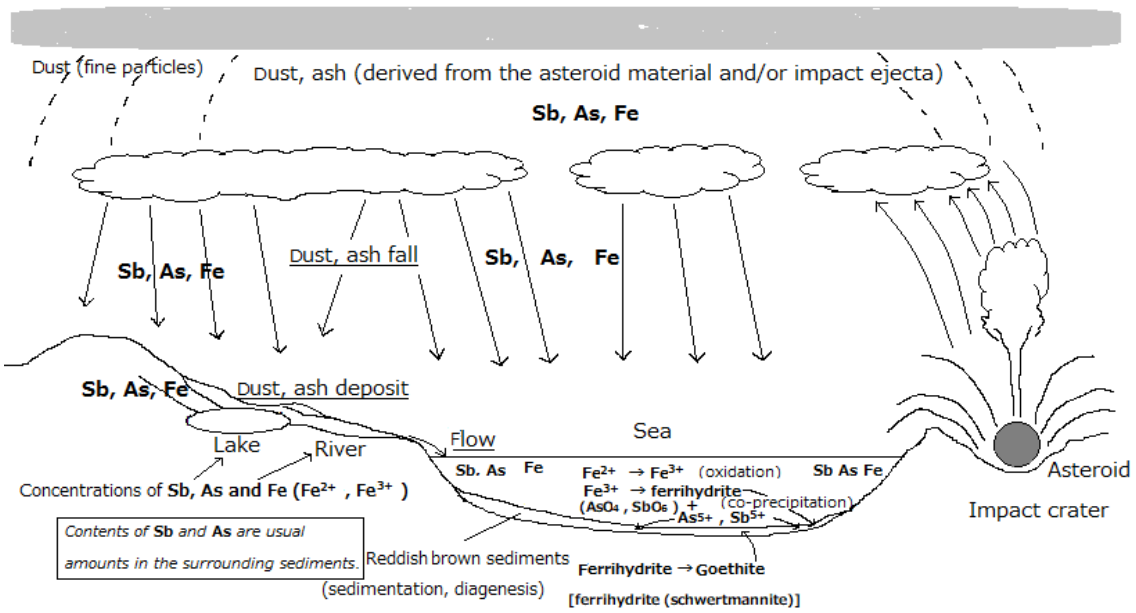


**Figure 4.5.** A schematic illustration showing concentration mechanism of Sb and As into deposits after the asteroid impact.

# 第 5 章 Chapter 5

# General Conclusion

General Conclusion

この学位論文では、結晶質相、非晶質・低結晶質相という多様な鉱物相において、浅熱水性の金・銀鉱床の形成メカニズムを考察する上で関連性のある 11 族元素の Cu, Ag, Au、15 族元素の As, Sb、16 族元素の Te、17 族（ハロゲン）元素の F に焦点を当て、最適、最新の分析・解析方法を用いて各種元素の詳細な情報を獲得した。そして、先行研究の再検討や新たな提案を交えて、議論を進めている。それに関して以下に章ごとにまとめる。

第 2 章

prosopite の結晶構造精密化と化学式の決定

Ca, Al の水酸基を含むフッ化物である prosopite は、その構造中の詳細な F と OH 間の固溶状態や order-disorder の関係に関して議論の余地がある鉱物である。よって、走査電子顕微鏡付属エネルギー分散型 X 線分光分析（SEM/EDS）法を用いて prosopite の化学組成を決定し、単結晶 X 線回折法を用いて詳細に水素原子位置を含む prosopite の精密結晶構造解析を行い、これらに関して考察した。prosopite の陽イオン席において、Al の一部が Cu と、Ca の一部が Sr と置換している試料が確認された。不純物の置換反応として、$Al^{3+} + (OH)^{-} \leftrightarrow Cu^{2+} + H_2O$ が考えられ、Cu のような遷移金属は鉱物の着色原因になっている。水素原子位置については、差フーリエ法を用いて残差電子密度ピークが現れる位置に決定した。その結果、prosopite 中の $F^{-}$ と $O^{2-}$ はそれぞれ F 席と O 席に規則分布している。ただ、化学分析と構造精密化から、(OH)席への $F^{-}$ の置換はわずかに起こるが、F 席への $(OH)^{-}$ の固溶は生じないと考えられる。よって、prosopite の化学構造式は、$CaAl_2F_4[(OH)_{4-x}F_x]$ ($x$ = 0.0–1.0)として表されることを新たに提案した。

第 3 章

petzite の結晶構造解析と XAFS 分析

petzite $Ag_3AuTe_2$ は、coloradoite HgTe や hessite $Ag_2Te$ と共生し、それらに連晶として産出する（Frueh, 1959）。Thompson (1948, 1949)は、petzite は、区別された規則的な位置に Ag 原子と Au 原子が配置されていることを示唆する明確な Ag-Au 比を持つ化合物であることを示している。それは calaverite $AuTe_2$ や sylvanite $(Ag,Au)_2Te_4$ とは異なり、3 次元の周期性、non-modulated (非変調)構造に対応している。本研究では、petzite 中の Au と Ag の order-disorder の関係のような構造の詳細と各元素の各々のサイトにおける席選択性、結合状態の特徴を明らかにすることが、主たる目的である。単結晶試料の精密構造解析から、本研究では先行研究の内容を確認したが、絶対構造は先行研究の Chamid et al. (1978)の旧モデルに関して対称（鏡像関係）である。Au $L_{III}$-edge XANES スペクトル解

析より、petzite の Au の化学結合は他の金鉱物のそれよりも明白にメタリックな特徴を持つ。また、Te $L_{III}$-edge XANES スペクトル解析より、petzite の Te の化学結合は部分的にイオン的特徴を示し、その原子価はメタリックと陰イオンの中間である。そして、petzite の Au, Ag, Te の、Debye-Waller factor を用いて見積もられた Debye 温度 $\theta_D$ は、それぞれ 73.3, 101.1, 108.5 K である。これらは、純金属において対応する値（それぞれ 178, 221, 152 K）よりもかなり低く、それぞれの金属についてのテルル化物中の異なる結合力を反映している。

第 4 章

隕石衝突時の特殊環境下で生成した堆積物（白亜紀-第三紀境界堆積物）( : 堆積物中の濃集元素、特に Sb, As の XAFS 解析と濃集過程の推定)

K-T 境界（白亜紀-第三紀地質年代境界）堆積物中には Ir のような白金族元素の他に Cr, Co, Ni, Cu, Zn, As, Sb といった元素も濃集していることが報告されている（Strong et al., 1987; Schmitz, 1992）が、非隕石起源によるところが大きく、火山活動（Officer and Drake, 1985）等と関連づけられて説明される (Zn), As, Sb の起源、濃集過程に関しては不明な点が多く、それらの元素の起源、濃集過程の詳細な議論のためには、元素が含まれる鉱物相やその形態を明らかにする必要がある。研究対象の Denmark の Stevns Klint の K-T 境界堆積層下部で Ir の含有量がピークである赤色堆積物中の主要構成鉱物は、X 線粉末回折分析では、smectite (montmorillonite), calcite, 少量の quartz, goethite であるが、他に同定困難な非晶質相や低結晶質成分が半分程度存在していると考えられる。よって、XAFS（X 線吸収微細構造）法を用いて、特に Sb, As の局所構造解析を行い、それらの化学的状態や配位環境に関する情報を得て、K-T 境界堆積物層中における Sb, As の形態および濃集鉱物相、また、濃集過程を議論した。

K-T 境界堆積物の Sb K-edge XANES（X 線吸収端近傍構造）スペクトルの形状とケミカルシフト（threshold energy の比較）、また、同様に As K-edge XANES スペクトルの形状とケミカルシフトから、Sb, As ともに+5 価で酸化物を形成している。そして、両元素とも ferrihydrite (schwertmannite)中の Sb と As と同様の局所構造を示す。また、Sb の XANES スペクトルと動径分布から、$SbO_6$ 八面体配位環境に置かれている。Sb は As と Fe イオンと共沈したと考えられ、(豊富な鉄水酸化物を生じている）K-T 境界堆積物の Sb と As は、沈殿作用と堆積作用を通して低結晶性の ferrihydrite (schwertmannite)に取り込まれていると考えられる。Sb と As の局所構造は Zr, Ti の局所構造（Tobase et al., 2015, 2019）のように隕石衝突時の直接的な情報を残していない。K-T 境界堆積物の Sb と As の局所構造と濃集過程は、鉱床付近等の土壌環境のそれと似ている。しかし、汚染地域のように局所的ではなく、世界各地に広く分布している K-T 境界堆積物のよ

うな通常でない環境下では、$Sb^{5+}$と $As^{5+}$の異常濃集が隕石衝突噴出物由来の塵や灰の降下によって広く汚染された地球環境の指標の一つになり得るだろう。

K-T 境界堆積物の Sb と As の濃集は、地表環境・酸化的状態で起こっており、熱水が関与した鉱床の形成過程とは異なる。Au-Sb, Pt-As の結合は観測されなかった。金鉱物の鉱化作用を議論する上で、関係する高温の熱水からの温度低下、そして、酸化環境下への変化の解明に向けて、高温熱水中での錯イオンの研究が必要である。

このように結晶質相の精密構造解析、主に非晶質・低結晶質相に対する局所構造解析と、含有元素に構造情報を与えることによって新たな知見が得られ、特殊な原子、イオンの構造・状態の解明や濃集過程・履歴の解読に成功した。

## 謝辞

この学位論文作成における研究に際して、多くの方々のご指導、ご援助を頂いた。

指導教官である吉朝朗教授には、研究全般において終始多大なご指導、ご援助を頂いた。また、高エネルギー加速器研究機構（KEK, Photon Factory）でのXAFS・単結晶 X 線回折実験、学会発表や国際誌への論文の投稿等、積極的に研究を行う機会を与えて頂き、成果を得ることができた。

熊本大学理学部地球環境科学講座の磯部博志教授には、室内実験（SEM/EDS, XRD 分析）をご指導、また、本研究において有益なご助言を頂いた。

そして、熊本大学理学部地球環境科学講座の西山忠男教授、渋谷秀敏教授、また、自然科学研究科物理科学講座の安仁屋勝教授には、本研究に対して多く議論して頂き、大変有益なご助言、ご指導を頂いた。

東北大学の杉山和正教授、奥部真樹准教授、総合科学研究機構の有馬寛博士、山口大学の中塚晃彦准教授、国立科学博物館の宮脇律郎博士、門馬綱一博士、北海道大学の佐藤努教授、フランス，ロレーヌ大学の Massimo Nespolo 教授には、実験、論文執筆において多大なご指導を頂いた。

また、元愛媛大学教授の皆川鉄雄博士には、野外調査において多くのご援助を頂いた。

北京高圧科学研究中心(HPSTAR)の鳥羽瀬翼博士、東北大学の徳田誠博士、および、吉朝研究室のメンバーには、実験、データ解析の他、議論の上で多大なご協力を頂いた。

熊本大学理学部地球環境科学講座の伴佳織様をはじめ皆様には、事務手続き等のご援助や激励を常に頂いた。

そして、両親には、いつも私の研究を温かく見守って頂き、また、健康管理に注意を払って頂いた。

以上の方々に深く感謝いたします。

**REFERENCES**

第 1 章

Kikuchi, Y., Matsugi, M. and Goto, T. (1982) Geological assessment and development of the Sakoshi-Odomari gold mine, Hyogo Prefecture. Mining Geology, 32, 361-368. (in Japanese).

Reed, M.H. and Spycher, N.F. (1984) Calculation of pH and mineral equilibria in hydrothermal waters with application to geothermometry and studies of boiling and dilution. Geochimica et Cosmochimica Acta, 48, 1479-1492.

Reed, M.H. and Spycher, N.F. (1985) Boiling, cooling, and oxidation in epithermal systems: A numerical modeling approach. Geology and Geochemistry of Epithermal Systems (Berger, B.R. and Bethke, P.M. eds.), Review in Economic Geology, 2, 249-272.

Seward, T.M. (1973) Thio complexes of gold and the transport of gold in hydrothermal ore solutions. Geochimica et Cosmochimica Acta, 37, 370-399.

Tobase, T., Yoshiasa, A., Komatsu, T., Maekawa, T., Hongu, H., Okube, M., Arima, H. and Sugiyama, K. (2019) Titanium local coordination environments in Cretaceous-Paleogene and Devonian-Carboniferous boundary sediments as a possible marker for large meteorite impact. Physics and Chemistry of Minerals, 46, 675-685.

他、第 2、3、4 章において、重複する引用文献は省略する。

第 2 章

Bailey, J.C. (1980) Formation of cryolite and other aluminofluorides: A petrologic review. Bulletin of the Geological Society of Denmark, 29, 1-45.

Brown, I.D. and Altermatt, D. (1985) Bond-valence parameters obtained from a systematic analysis of the inorganic crystal structure database. Acta Crystallographica, B41, 244-247.

Giacovazzo, C. and Menchetti, S. (1969) The crystal structure of prosopite. Naturwissenschaften, 56, 86-87.

Higashi, T. (1995) ABSCOR. Rigaku Corporation, Tokyo, Japan.

International Tables for Crystallography, Volume C (1992). Wilson, A.J.C., Ed. Kluwer Academic Publishers, Dordrecht.

Jinnouchi, S., Yoshiasa, A., Sugiyama, K., Simura, R., Arima, H., Momma, K. and Miyawaki, R. (2016) Crystal structure refinements of legrandite, adamite, and

paradamite: The complex structure and characteristic hydrogen bonding network of legrandite. Journal of Mineralogical and Petrological Sciences, 111, 35-43.

Momma, K. and Izumi, F. (2011) VESTA 3 for three-dimensional visualization of crystal, volumetric and morphology data. Journal of Applied Crystallography, 44, 1272-1276.

Palache, C., Berman, H. and Frondel, C. (1951) Dana's System of Mineralogy, seventh edition, 2. John Wiley, New York, 121-123.

Pudovkina, Z.V., Chernitsova, N.M. and Pyatenko, Yu.A. (1973) Refinement of the crystalline structure of prosopite $CaAl_2F_4(OH)_4$. Journal of Structural Chemistry, 14, 345-347.

Scheerer, Th. (1857) Mineralogische Charakteristik des Prosopit. Annalen der Physik, 177, 361-386.

Shannon, R.D. (1976) Revised effective ionic radii and systematic studies of interatomic distances in halides and chalcogenides. Acta Crystallographica, A32, 751-767.

Sheldrick, G.M., (1997) SHELXL97, Program for the Refinement of Crystal Structure; University of Göttingen, Göttingen, Germany.

Young, B., Ryback, G., Braithwaite, R.S.W. and Francis, J.G. (1997) Prosopite, doyleite and otavite from Coldstones Quarry, Pateley Bridge, North Yorkshire. Mineralogical Magazine, 61, 895-897.

第 3 章

Alvarez, S. (2013). *Dalton Trans*. **42**, 8617-8636.

Bindi, L., Arakcheeva, A. & Chapuis, G. (2009). *Am. Mineral*. **94**, 728-736.

Bindi, L. & Chapuis, G. (2017). *Aperiodic Mineral Structures*. In *Mineralogical Crystallography*. *EMU Notes in Mineralogy*, Vol. 19, edited by J. Plasil, J. Majzlan and S. Krivovichev. London: European Mineralogical Union and Mineralogical Society of Great Britain and Ireland.

Busing, W. R. & Levy, H. A. (1957). *Acta Cryst*. **10**, 180-182.

Chamid, S., Pobedimskaya, E.A., Spiridonov, E.M. & Belov, N.V. (1978). *Sov. Phys. Crystal*., **23**, 267-269.

Christensen, M., Lock, N., Overgaard, J., & Iversen, B.B. (2006). *J. Am. Chem. Soc*. **128**, 15657-15665.

Cordero, B., Gómez, V., Platero-Prats, A.E., Revés, M., Echeverría, J., Cremades, E., Barragán F. and Alvarez, S. (2008). *Dalton Trans*. **21**, 2832-2838.

Flack, H. D. (1983). *Acta Cryst*. **A39**, 876-881.

Frueh, A.J. (1959). The crystallography of petzite, $Ag_3AuTe_2$. *Am. Mineral*. **44**, 693-701.

Hiratoko, T., Yoshiasa, A., Nakatani, T., Okube, M., Nakatsuka, A. & Sugiyama, K. (2013). Temperature dependence of pre-edge feature in Ti K-edge XANES spectra for $ATiO_3$ (A= Ca and Sr), $A_2TiO_4$ (A=Mg and Fe), $TiO_2$ rutile and $TiO_2$ anatase. *J. Synchrotron. Rad.*, **20**, 641-643.

Hongu, H., Yoshiasa, A., Teshima, A., Isobe, H., Sugiyama, K., Arita, H., Nakatsuka, A., Momma, K. & Miyawaki, R. (2018). Crystal structure refinement and chemical formula of prosopite, $CaAl_2F_4[(OH)_{4-x}F_x]$ x = 0.0-1.0. *J. Mineral. Petrol. Sci*. **113**, 152-158.

Momma, K. & Izumi, F. (2011). VESTA 3 for three-dimensional visualization of crystal, volumetric and morphology data. *J. Appl. Cryst*. **44**, 1272-1276.

Nakatsuka, A., Shimokawa, M., Nakayama, N., Ohtaka, O., Arima, H., Okube, M. & Yoshiasa, A. (2011). *Am. Mineral*. **96**, 1593-1605.

Nespolo, M., Aroyo, M.I. & Souvignier, B. (2018). *J. Appl. Cryst*. **51**, 1481-1491.

Okudera, H., Yoshiasa, A., Murai, K., Okube, M., Takeda, T. & Kikkawa, S. (2012). Local structure of magnetite and maghemite and chemical shift in Fe K-edge XANES. *J. Mineral. Petrol. Sci*. **107**, 127-132.

Pertlik F. (1984). Kristallchemie naturlicher telluride III: Die kristallstruktur des minerals calaverit, $AuTe_2$. *Z. Kristallogr*. **169**, 227-236.

Petricek, V., Dusek, M. & Palatinus L. (2014). *Z. Kristallogr*. **229**, 345-352.

Reithmayer, K., Steurer, W., Schulz, H. & de Boer, J.L. (1993). High-pressure single-crystal structure study on calaverite, $AuTe_2$. *Acta Cryst*. **B49**, 6-11.

Schneider, J. & Schulz, H. (1993). *Z. Kristallogr*. **203**, 1-15.

Schutte, W.J. & de Boer, J.L. (1988). Valence fluctuations in the incommensurately modulated structure of calaverite $AuTe_2$. *Acta Cryst*. **B44**, 486-494.

Shannon, R. D. (1981). *Structure and Bonding in Crystals*, Vol. 2, edited by M. OBonding in Crystalsmensurately-70. New York: Academic Press.

Thompson, R.M. (1948). Pyrosyntheses of telluride minerals. *Am. Mineral*. **33**, 209-210.

Thompson, R.M. (1949). Telluride minerals and their occurrence in Canada. *Am Mineral*. **34**, 350-353.

Tobase, T., Yoshiasa, A., Hiratoko, T. & Nakatsuka, A. (2018). Rutile and anatase types of temperature dependent pre-edge peak intensities in K-edge XANES spectra for AO (A=Mn), $A_2O_3$ (A=Sc,Cr and Mn), and $AO_2$ (A= Ti and V). *J. Synchrotron Rad*. **25**, 1129-1134.

Tokuda, M., Yoshiasa, A., Mashimo, T., Iishi, K. & Nakatsuka, A. (2018). *Acta Cryst*. **C74**, 460-464.

Tunell, G. (1941). The atomic arrangement of sylvanite. *Am*. *Mineral*. **26**, 457-477.

Venudhar, Y.C., Iyengar, L. & Krishna Rao, K.V. (1978). *J*. *Less-Common Met*. **60**, 41-46.

Willis, B.T.M. & Pryor, A.W. (1975). *Thermal Vibrations in Crystallography*. Cambridge University Press.Wood, I. G., Knight, K. S., Price, G. D. & Stuart, J. A. (2002). *J*. *Appl*. *Cryst*. **35**, 291-295.

Wyckoff, R.W.G. (1963). *Cryst*. *Struct*. **1**, 7-83.

Yoshiasa, A., Kitahara, G., Tobase, T., Hiratoko, T., Hongu, H., Nakatani, T. & Murai, K. (2018). Determination of Ferro- and Antiferroelectricity Using the Temperature Dependence of the Pre-Edge Features in the XANES Spectra: XANES Study of Tetragonal and Cubic $ATiO_3$ (A= Sr, Ba, and Pb) and $PbZrO_3$. *Phys*. *Status Solidi B*, **255**, 1800050.

Yoshiasa, A., Nakatani, T., Nakastuka, A., Okube, M., Sugiyama, K. & Mashimo, T. (2016). *Acta Cryst*. **B72**, 381-388.

第 4 章

Alvarez, L.W., Alvarez, W., Asaro, F. and Michel, H.V. (1980) Extraterrestrial cause for the Cretaceous-Tertiary extinction. Science, 208, 1095-1108.

Drits, V.A., Lindgreen, H., Sakharov, B.A., Jakobsen, H.J. and Zviagina, B.B. (2004) The detailed structure and origin of clay minerals at the Cretaceous/Tertiary boundary, Stevns Klint (Denmark). Clay Minerals, 39, 367-390.

Ebihara, M. and Miura, T. (1996) Chemical characteristics of the Cretaceous-Tertiary boundary layer at Gubbio, Italy. Geochimica et Cosmochimica Acta, 60, 5133-5144.

Filella, M., Belzile, N. and Chen, Y.-W. (2002) Antimony in the environment: a review focused on natural waters:I. Occurrence. Earth-Science Reviews, 57, 125-176.

Fukushi, K., Sato, T. and Yanase, N. (2003a) Solid-solution reactions in As(V) sorption by schwertmannite. Environmental Science and Technology, 37, 3581-3586.

Fukushi, K., Sasaki, M., Sato, T., Yanase, N., Amano, H. and Ikeda, H. (2003b) A natural attenuation of arsenic in drainage from an abandoned arsenic mine dump. Applied Geochemistry, 18, 1267-1278.

Gilmour, I. and Anders, E. (1989) Cretaceous-Tertiary boundary event: Evidence for a short time scale. Geochimica et Cosmochimica Acta, 53, 503-511.

Grew, E.S., Barbier, J., Britten, J., Hålenius, U. and Shearer, C.K. (2007) The crystal

chemistry of welshite, a non-centrosymmetric (*P*1) aenigmatite-sapphirine-surinamite group mineral. American Mineralogist, 92, 80-90.

Huminicki, D.M.C. and Hawthorne, F.C. (2001) Refinement of the crystal structure of swedenborgite. Canadian Mineralogist, 39, 153-158.

Maeda, H. (1987) Accurate bond length determination by EXAFS method. Journal of the Physical Society of Japan, 56, 2777-2787.

Mitsunobu, S., Harada, T. and Takahashi, Y. (2006) Comparison of antimony behavior with that of arsenic under various soil redox conditions. Environmental Science & Technology, 40, 7270-7276.

Mitsunobu, S., Takahashi, Y., Terada, Y. and Sakata, M. (2010) Antimony(V) incorporation into synthetic ferrihydrite, goethite, and natural iron oxyhydroxides. Environmental Science & Technology, 44, 3712-3718.

Mitsunobu, S., Muramatsu, C., Watanabe, K. and Sakata, M. (2013) Behavior of antimony(V) during the transformation of ferrihydrite and its environmental implications. Environmental Science & Technology, 47, 9660-9667.

Miyano, Y., Yoshiasa, A., Tobase, T., Isobe, H., Hongu, H., Okube, M., Nakatsuka, A. and Sugiyama, K. (2016) Weathering and precipitation after meteorite impact of Ni, Cr, Fe, Ca and Mn in K-T boundary clays from Stevns Klint. Journal of Physics: Conference Series, 712, 012097, doi: 10.1088/1742-6596/712/1/012097.

Officer, C.B. and Drake, C.L. (1985) Terminal Cretaceous environmental events. Science, 227, 1161-1167.

Okube, M., Sasaki, S., Yoshiasa, A., Wang, L., Nakatani, T., Hongu, H., Murai, K., Nakatsuka, A. and Miyawaki, R. (2012) Local structure of Zn in Cretaceous-Tertiary boundary clay from Stevns Klint. Journal of Mineralogical and Petrological Sciences, 107, 192-196.

Sakai, S., Yoshiasa, A., Arima, H., Okube, M., Numako, C. and Sato, T. (2007) XAFS study of As in K-T boundary clay. The American Institute of Physics, Conference Proceeding, 882, 274-276.

Schmitz, B. (1985) Metal precipitation in the Cretaceous-Tertiary boundary clay at Stevns Klint, Denmark. Geochimica et Cosmochimica Acta, 49, 2361-2370.

Schmitz, B. (1992) Chalcophile elements and Ir in continental Cretaceous-Tertiary boundary clays from the western interior of the USA. Geochimica et Cosmochimica Acta, 56, 1695-1703.

Shannon, R.D. (1976) Revised effective ionic radii and systematic studies of interatomic distances in halides and chalcogenides. Acta Crystallographica, A32, 751-767.

Strong, C.P., Brooks, R.R., Wilson, S.M., Reeves, R.D., Orth, C.J., Mao, X.-Y.,

Quintana, L.R. and Anders, E. (1987) A new Cretaceous-Tertiary boundary site at Flaxbourne River, New Zealand: Biostratigraphy and geochemistry. Geochimica et Cosmochimica Acta, 51, 2769-2777.

Tobase, T., Yoshiasa, A., Wang, L., Hiratoko, T., Hongu, H., Okube, M. and Sugiyama, K. (2015) XAFS study of Zr in Cretaceous-Tertiary boundary clays from Stevns Klint. Journal of Mineralogical and Petrological Sciences, 110, 88-91.

Vink, B.W. (1996) Stability relations of antimony and arsenic compounds in light of revised and extended Eh-pH diagrams. Chemical Geology, 130, 21-30.

Wilson, S.C., Lockwood, P.V., Ashley, P.M. and Tighe, M. (2010) The chemistry and behaviour of antimony in the soil environment with comparisons to arsenic: a critical review. Environmental Pollution, 158, 1169-1181.

Yoshiasa, A., Nagai, T., Ohtaka, O., Kamishima, O. and Shimomura, O. (1999) Pressure and temperature dependence of EXAFS Debye-Waller factors in diamond type and white-tin type germanium. Journal of Synchrotron Radiation, 6, 43-49.

Zedlitz, O. (1932) Die kristallstruktur von romeit und schneebergit. Zeitschrift für Kristallographie, 81, 253-263.